ABSTRACT

CHARACTERIZATION OF BORON/IRON-OXIDE CORE/SHELL STRUCTURE FOR BORON NEUTRON CAPTURE THERAPY BY STEM/EELS-XEDS AND MÖSSBAUER SPECTROSCOPY

Mason Hayward, M.S.
Department of Physics
Northern Illinois University, 2019
Yasuo Ito, Director

Boron/iron-oxide core/shell structured nanoparticles were characterized for application in boron neutron capture therapy (BNCT). BNCT is a cancer treatment method using the ability of boron to absorb thermal neutrons and a proposed drug delivery system utilizing an external magnetic field to direct the boron nanoparticles to targeted cancer sites and to extract the used nanoparticles after treatment. Boron nanoparticles were magnetically functionalized by encapsulating with an iron oxide shell. As such the exact composition, size distribution and oxidation states of the core/shell structures can affect treatment efficacy. Characterization was done by electron energy loss spectroscopy (EELS) and x-ray energy dispersive spectroscopy (XEDS) within the scanning transmission electron microscope. Magnetic and additional electronic characterizations of the iron-oxide nanoparticles were performed by Mössbauer spectroscopy, whose results were compared with those of EELS Fe L_{23} peak ratio. Both the EELS and Mössbauer spectroscopy results indicated a mixed valence state, indicative of Fe_3O_4, for the iron-oxide nanoparticles. EELS analysis was performed on pure boron nanoparticles to show initial purity and create a spectrum reference for the core/shell structured nanoparticles. XEDS on the boron/iron oxide nanoparticles

indicated the formation of the core/shell structure and EELS revealed the Fe_3O_4 structure is maintained along with the purity of the boron core.

NORTHERN ILLINOIS UNIVERSITY
DE KALB, ILLINOIS

MAY 2019

CHARACTERIZATION OF BORON/IRON-OXIDE CORE/SHELL STRUCTURE FOR BORON NEUTRON CAPTURE THERAPY BY STEM/EELS-XEDS AND MÖSSBAUER SPECTROSCOPY

BY

MASON HAYWARD

A THESIS SUBMITTED TO THE GRADUATE SCHOOL
IN PARTIAL FULFILLMENT OF THE REQUIREMENTS
FOR THE DEGREE
MASTER'S OF SCIENCE

DEPARTMENT OF PHYSICS

Thesis Director:
Yasuo Ito

ACKNOWLEDGEMENTS

I would like to first and foremost thank Dr. Yasuo Ito, my thesis advisor, for everything he's done during my time at Northern Illinois Univeristy. He was not only instrumental in my learning of the electron microscope and the associated analytical techniques, but he helped to push me to grow as a researcher and scientist. Thanks to Dr. Dennis Brown for his collaboration on the Mössbauer data collection and analysis portion of this project. Without his help, Mössbauer confirmation of the iron oxide nanoparticles would have been nigh impossible. I would also like to thank Dr. Narayan Hosmane whose overall BNCT research is what fueled the need for this thesis project. As I am not synthesis chemist, I want to acknowledge John Wozny and Dr. Eyrusalam Bedasso for his much needed collaboration in the nanoparticle synthesis. For his design of the LaTeX document that follows NIU graduate school guidelines, I want to thank Dr. Roland Winkler for saving me an exorbitant amount of time on formatting.

I would like to thank Dr. Jianguo Wen (ANL CNM) and Dr. Nestor Zaluzec (ANL Photon Science) for their guidance and assistance with the electron microscopes. Most notably, I was to acknowledge Argonne National Laboratory and the Center for Nanoscale Materials for the acceptance of the proposal and the usage of the electron microscopes that made this research possible.

Thank you Elliot Parrish and Rafa Oreamuno for helping me stay on track with this project and future Ph.D. applications. I definitely remember more physics now after our lengthy discussions while studying for classes and qualifier exams. Also thank you Elliot for helping me debug code even when I wasn't sure what I needed it to do. To Group 3, you

guys were and continue to be an excellent distraction from the stress of graduate school and I'll forever cherish what we've accomplished.

Amanda Tyrcha, thank you for all your support and constant reminders that I am capable of finishing. It's been a roller coaster of a journey and I wouldn't want to do it without you.

Most importantly, I want to thank my family, Dad, Julia, Susie, and Lori. Your continued support of me helped push me to become the person I am today. There's no amount of words that can express the gratitude I have for you and all your help.

Use of the Center for Nanoscale Materials, an Office of Science user facility, was supported by the U.S. Department of Energy, Office of Science, Office of Basic Energy Sciences, under Contract No. DE-AC02-06CH11357.

DEDICATION

To my mother, Candice Hayward. Hope I'm doing you proud.

TABLE OF CONTENTS

Page

LIST OF TABLES vii

LIST OF FIGURES. viii

LIST OF APPENDICES xi

LIST OF SYMBOLS xii

Chapter

1 INTRODUCTION 1

1.1 Scattering Theory 2

1.1.1 Elastic Scattering 2

1.1.2 Inelastic Scattering 3

1.2 Spectroscopy. 5

1.2.1 Electron Energy Loss Spectroscopy. 5

1.2.2 Energy Dispersive X-Ray Spectroscopy 9

1.2.3 Mössbauer Spectroscopy 12

1.3 Thesis Goals 14

2 EXPERIMENTAL 15

2.1 Instrumentation 15

2.1.1 TEM/STEM 15

2.1.2 XEDS 18

2.1.3 EELS 20

2.1.4 Mössbauer Spectroscopy 22

Chapter Page

2.2 Samples . . . 23
2.2.1 Iron Oxide Nanoparticles . . . 24
2.2.2 Boron Nanoparticles . . . 25
2.2.3 Boron/Iron oxide Nanoparticle (Core/Shell Structure) . . . 26
3 RESULTS AND DISCUSSION . . . 27
3.1 Analysis of Iron Oxide Nanoparticles . . . 27
3.1.1 EELS . . . 28
3.1.2 Mössbauer Analysis . . . 32
3.1.3 Summary . . . 34
3.2 Analysis of Boron/Iron oxide Nanoparticle . . . 35
3.2.1 Pure Boron Nanoparticle . . . 35
3.2.2 Core/Shell Structure . . . 36
3.2.2.1 XEDS . . . 37
3.2.2.2 EELS . . . 41
3.2.3 Summary . . . 43
4 CONCLUSIONS AND FUTURE WORK . . . 44
REFERENCES . . . 45
APPENDICES . . . 48

LIST OF TABLES

Table Page

3.1 Calculated L_3/L_2 intensity ratios for the iron oxide nanoparticle sample. . . . 30

3.2 Summary of Mössbauer Analysis showing the magnetic fields and isomer shifts of each site fit. 33

LIST OF FIGURES

Figure Page

1.1 Example zero (I_0) and low loss (I_p) peaks within the low loss region [10]. . . . 6

1.2 Example of core loss region with labeled core loss edges.. . . . 8

1.3 Diagram showing the nomenclature for core loss edges [10].. . . . 9

1.4 Atomic model showing the emission of a characteristic x-ray when a higher energy electron fills a vacancy of a lower energy shell. The energy of the x-ray is quantified as the difference of the initial (ϕ_i) and final shell(ϕ_f): $E_{x-ray} = \phi_i - \phi_f$ [11]. . . . 10

1.5 Allowed transitions that result in K, L, and M characteristic x-rays [10]. . . . 11

1.6 Diagram showing the hyperfine parameters and their effect on the Mössbauer spectrum [15].. . . . 13

2.1 Detector setup for analytical electron microscope [18]. . . . 17

2.2 Example XEDS spectra plotting x-ray count vs. x-ray energy (keV). . . . 18

2.3 Visualization of the data cube. In relation to XEDS, the XY plane represents the pixel location with the Z-axis representing the spectrum generated at the specific pixel [10]. . . . 19

2.4 Example XEDS mapping showing the elemental distribution of iron (red), boron (green), and oxygen (blue).. . . . 20

2.5 Example plots showing the initial spectrum, background fit, and background subtracted spectrum for boron, oxygen, and iron (Left to right). . . . 21

2.6 Arctan fit used to analyze the L_3/L_2 to quantify the valence structure of the iron oxide. . . . 21

2.7 Mössbauer Calibration data. . . . 23

2.8 Bright field image of the initial high concentration iron oxide sample. . . . 25

Figure Page

3.1 HAADF image of pure iron oxide nanoparticle cluster. 27

3.2 Hybridization of oxygen s-orbital and iron p-orbitals. 28

3.3 EELS spectrum of Iron L-edges collected from iron oxide sample. Each spectrum is labeled for reference. 29

3.4 Left: Oxygen K-edge of analyzed iron oxide nanoparticles. Right: Oxygen K-edge for different transition metal oxides [21] 31

3.5 Overview of Fe_3O_4 A and B sites within the crystal structure [22].. 32

3.6 Mössbauer spectrum of Fe_3O_4 showing 3-site fit. Site 1 (red) corresponds to the Fe^{3+} within the A-site. Site 3 (blue) corresponds to the Fe^{3+}/Fe^{2+} B-site and Site 2 (green) is Fe^{3+} in a nonmagnetic state. 33

3.7 Mössbauer spectrum of quadrupole doublet indicative of superparamagnetism. 34

3.8 HAADF image of a boron nanoparticle cluster. 35

3.9 (Left) EELS spectra of analyzed boron nanoparticles. (Right) Analyzed boron K-edges from pure boron (a), B_2O_3 (b), and t-Ni_2B (c) [23]. 36

3.10 HAADF image of boron/iron nanoparticle cluster hanging at the edge of the carbon film. 37

3.11 XEDS mapping of boron/iron oxide nanoparticle cluster showing the presence of boron, iron, and oxygen. 38

3.12 XEDS Mapping of iron and boron in the core/shell nanoparticle structure.. . 38

3.13 XEDS mapping of iron and oxygen in the core/shell nanoparticle structure. . 39

3.14 XEDS mapping of boron and oxygen in the core/shell nanoparticle structure. The large presence of oxygen indicates possible oxidation of the boron core. . 39

3.15 XEDS mapping of boron/iron oxide nanoparticle cluster. 40

3.16 XEDS spectrum of boron/iron oxide nanoparticle cluster. Insert: Spectrum location on XEDS mapping 41

3.17 EELS spectrum of core/shell structure with labeled edges. Insert: Oxygen K-edge and Iron L-edges 42

Figure Page

B.1 EDS Mapping of nanoparticle cluster with iron (red) and oxygen (blue) shown. The high presence of oxygen indicates a possibility of oxidation within the core.. 51

B.2 EDS Mapping of nanoparticle cluster with boron (green) and iron (red) shown. The iron appears to coat the boron in this mapping indicating the presence of a core/shell structure.. 52

B.3 EDS Mapping of small nanoparticle cluster with boron (green) and oxygen (blue) shown. A high presence of oxygen also contained in this mapping indicating possible oxidation. 53

B.4 EDS Mapping of small nanoparticle cluster with boron (green) and iron (red) shown. 5 individual core/shell structures are readily visible from this cluster. 54

B.5 EDS Mapping of small nanoparticle cluster with iron (red) and oxygen (blue) shown. Oxygen presence surrounding the entirety of the core/shell structure indicating possible oxidation of core.. 55

B.6 EDS Mapping of nanoparticle cluster with boron (green) and oxygen (blue) shown. Non-uniform distribution of boron is readily visible across this nanoparticle cluster. 56

B.7 EDS Mapping of nanoparticle cluster with iron (red) and oxygen (blue) shown. Non-uniform presence of oxygen in regards to oxygen indicates possible oxidation of core. The iron shell also exhibits a non-uniformity. 57

B.8 EDS Mapping of nanoparticle cluster with boron (green) and oxygen (blue) shown. Oxygen distribution indicates a localization to the shell of the nanoparticle structure.. 57

LIST OF APPENDICES

Appendix Page

A SOFTWARE 48

B ADDITIONAL EDS SPECTRUM 50

LIST OF SYMBOLS

BNCT	Boron Neutron Capture Therapy
B_10H_14	Decaborane
CCD	Charged Coupled Device
EELS	Electron Energy Loss Spectroscopy
eV	electron volt
Fe_3O_4	Iron oxide structure commonly referred to as magnetite
FEG	Field Emission Gun
GOS	Generalized Oscillator Strength
HAADF	High Angle Annular Dark Field
FWHM	Full width at half maximum
LaB_6	Lanthanum hexaboride
MDT	Magnetic Drug Targeting
NH_4OH	Ammonium Hydroxide
nm	nanometer (10^{-9} meters)
SDD	Silicon Drift Detector
SNR	Signal-to-Noise Ratio
(S)TEM	(Scanning) Transmission Electron Microscope
XEDS	X-ray Energy Dispersive Spectroscopy
ZLP	Zero loss peak

CHAPTER 1

INTRODUCTION

Boron neutron capture therapy (BNCT) is a cancer therapy technique that involves introducing boron-10 to a tumor site then irradiating them with thermal neutrons. The boron-11 undergoes rapid fission of boron-11 atoms into an α-particle, Li-7 atom and an emitted γ-ray described in Equation 1.1 [1].

$$^{10}B +^{1} n \rightarrow^{7} Li^{3+} +^{4} He^{2+} + \gamma + 2.4MeV \tag{1.1}$$

The α-particles ($^{4}He^{2+}$) and Li-7 travel approximately the diameter of a singular cell which defines the localization of cellular destruction. One proposed method of boron delivery to tumorous cells is the use of magnetic nanoparticles (Magnetic Drug Targeting, MDT). Iron oxide nanoparticles have proven to be a viable drug carrier due to their inherent magnetic properties [2]. As such, boron/iron oxide core/shell nanoparticles are an excellent candidate for BNCT [3]. Analysis of these particles is required to ensure compatibility for BNCT as a core/shell structure of pure boron/Fe_3O_4 below a size of 50nm is desired. Bulk characterization is not entirely encompassing for analyzing these core/shell structures. The use of the scanning transmission electron microscope (STEM) allows for localized nanoscale characterization. Within the electron microscope, electron energy loss spectroscopy (EELS) and x-ray energy dispersive spectroscopy (XEDS) was used to quantitatively and qualitatively determine nanoscale characteristics. Mössbauer spectroscopy, a bulk analytical technique that uses resonantly emitted γ-rays, can also be used to probe electronic structure to independently confirm results from the electron microscope.

In the following sections, the theory behind the electron-matter interactions occurring in the STEM is reviewed. Along with this, an introduction to the high angular annular dark field imaging (HAADF), EELS and XEDS and their mechanisms are discussed.

1.1 Scattering Theory

The interaction of electrons with matter is the core concept for the imaging and analytical methods in the electron microscope. When the electrons scatter off the sample, two types of scattering can occur: elastic and inelastic. In this section, derivation and important concepts of the scattering process used in the STEM and related spectroscopic techniques are expanded on.

1.1.1 Elastic Scattering

Elastic scattering is due to the Coulomb interaction with the atomic nucleus. Incident electrons that pass near enough to the atomic nuclei are scatted at high angles, referred to as Rutherford scattering [4]. For these Rutherford scattering processes, the differential cross-section can be initially defined as:

$$\frac{d\sigma}{d\Omega} = |f(\theta)|^2 \tag{1.2}$$

where $\frac{d\sigma}{d\Omega}$ is the differential cross-section and $f(\theta)$ is the scattering amplitude as a function of scattering angle (θ). As the elastic scattering model is the same as Rutherford's model for alpha particles, the differential cross-section becomes:

$$\frac{d\sigma}{d\Omega} = \left(\frac{2\gamma Z}{a_0 q^2}\right)^2 \tag{1.3}$$

Z is the atomic number, γ is the relativistic factor ($\sqrt{1-\frac{v^2}{c^2}}$), and $a_0 = .529\ \mathring{A}$ is the Bohr radius. The scattering vector, q, is defined in terms of the incident wave vector (k_0) and the scattering angle, such that q = $2k_0\sin(\frac{\theta}{2})$. When the differential cross-section is integrated between a minimum and maximum scattering angle (θ_{min} and θ_{max}), the total cross-section results in

$$\sigma_d = (.250barn)FZ^2\left(\frac{sin^2(\frac{\theta_{max}}{2})}{sin^2(\frac{\theta_{min}}{2})-1}\right) \tag{1.4}$$

with barn is $10^{-28}m^2$, $F = \frac{1-v^2/c^2}{v^4/c^4}$ This total cross section can be directly related to the signal (I_d) received at high angles when an electron beam (I) passes through the sample with an area density of N atoms per unit area:

$$I_d = NI\sigma_d = NI(.250barn)FZ^2\left(\frac{sin^2(\frac{\theta_{max}}{2})}{sin^2(\frac{\theta_{min}}{2})-1}\right) \tag{1.5}$$

This relation between the signal received and the cross-section results in the Z^2 correlation that occurs in the high angle annular dark-field detector.

1.1.2 Inelastic Scattering

Inelastic scattering occurs when the electron beam interacts electrostatically within the inner and outer shell electrons. This causes a noticeable energy transfer. The resulting inelastic differential scattering cross-section ($\frac{d\sigma_i}{d\Omega}$) can be written in a form similar to that of the elastic scattering differential cross-section modified by an inelastic factor

$$\frac{d\sigma_i}{d\Omega} = \frac{4\gamma^2 Z}{{a_0}^2 q^4}\frac{k_1}{k_0}|\epsilon_n(q)|^2 \tag{1.6}$$

here k_0 and k_1 are the wave vector magnitudes of the electron before and after the scattering event. The first term is similar to Rutherford scattering when Z = 1 due to the interaction with a single electron. The final term ($|\epsilon_n(q)|^2$) is a dimensionless inelastic factor property of the target atom. The GOS is the response of the atom when an external source supplies energy and momentum [4]. The GOS is given by

$$f_n(q) = \frac{E_n}{R}\frac{|\epsilon_n(q)|^2}{(qa_0)^2} \tag{1.7}$$

where R is the Rydberg energy (13.6eV) and E_n is the transition energy change [5]. This inelastic factor can be written in terms of the generalized oscillator strength (GOS) and substituted into the differential cross section, resulting in the form of

$$\frac{d\sigma_d}{d\omega} = \frac{4\gamma^2 R}{E_n q^2}\frac{k_1}{k_0}f_n(q) \tag{1.8}$$

here $\frac{k_1}{k_0} \approx 1 - 2E_n(m_0v^2)^{-1}$. This differential cross-section is currently only in terms of varying angle, but not energy dependence. Therefore, the GOS should be defined as a continuous function of E. This gives a double differential cross-section defined by:

$$\frac{d^2\sigma}{d\Omega dE} = \frac{4\gamma^2 R k_1}{E q^2 k_0}\frac{df}{dE}(q, E) \tag{1.9}$$

Eq. 1.9 still lacks the scattering angle dependence desired. This can be resolved by relating q to θ using the relation $q^2 \approx k_0^2(\theta^2 + \theta_E^2)$. θ_E is the characteristic scattering angle and can be calculated through the following definition:

$$\theta_E = \frac{E}{(E_0 + m_0c^2)(\frac{v}{c})^2} \tag{1.10}$$

This relation when substituted into equation 1.9 gives the final differential cross-section in terms of θ and energy.

$$\frac{d^2\sigma}{d\Omega dE} = \frac{4\gamma^2 R}{E{k_0}^2}\left(\frac{1}{\theta^2+\theta_E^2}\right)\frac{df}{dE} \tag{1.11}$$

where k_1/k_0 is approximately 1, which occurs when energy loss in the incident electron $<<$ E_0), and $q^2 \approx {k_0}^2(\theta^2+\theta_E^2)$.

1.2 Spectroscopy

Spectroscopy is the study of the interaction of matter with electromagnetic radiation [6]. Three different types of spectroscopic techniques were used within this study to analyze nanoparticle samples, electron energy loss spectroscopy, energy dispersive x-ray spectroscopy, and Mössbauer spectroscopy. In this section, each spectroscopic technique will be expanded on.

1.2.1 Electron Energy Loss Spectroscopy

Electron energy loss spectroscopy is the spectroscopic technique used when electrons are allowed to interact with a sample and the resulting transmitted scattered electrons are analyzed to give an energy spectrum [7]. Depending on the scattering mechanism in the electron shells, the scattering probability varies. Intensity versus energy loss can be plotted as a spectrum. This spectrum contains two regions of interest, the zero and low loss region and the core loss region.

Zero and Low Loss Region. Within the energy loss spectrum, the most intense feature will be the zero loss peak (ZLP) as seen in Figure 1.1. This peak represents the intensity of elastic or unscattered electrons. Also contained in this peak are electrons scattered through phonon interactions, lattice vibrations [8], which result in a ΔE between 10-100meV. Information contained within the ZLP is the full width at half maximum of the peak which correlates to the energy dispersion of the electron source and energy resolution of the EELS spectrometer [7].

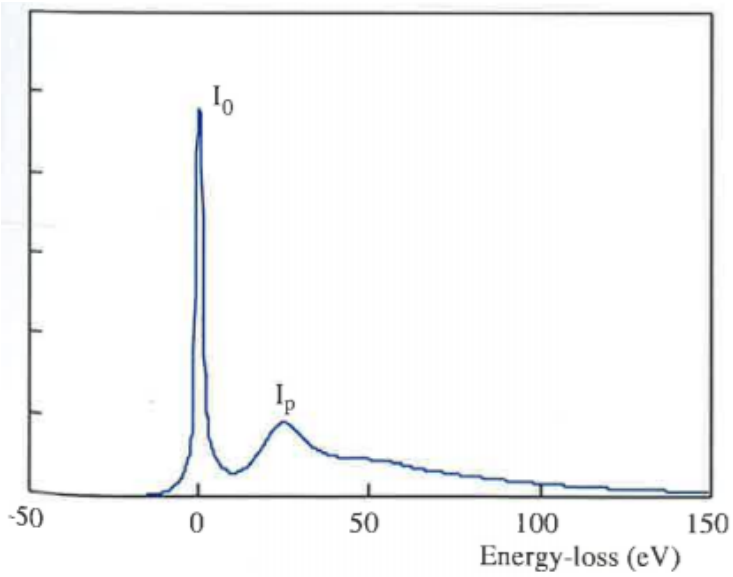

Figure 1.1: Example zero (I_0) and low loss (I_p) peaks within the low loss region [10].

The low loss peak occurs between 0-50eV and is often referred to as the plasmon peak. This is due to incident electrons exciting plasmons, collective oscillations of the valence electrons [8]. It is expected that there is at least one intense plasmon peak as plasmon mean free path (λ_p) is approximately 100nm [7, 10]. Multiple peaks can occur if the thickness (t) of the sample is larger than λ_p. The plasmon peak can be used to make thickness measurements

if the intensity of the plasmon peak (I_p), λ_p and the ZLP intensity (I_0) are also known [10]. Thickness can be calculated using:

$$t = \lambda_p \left(\frac{I_p}{I_0} \right) \tag{1.12}$$

Other information contained within the plasmon peak is the relationship between the energy of the plasmon peak and the density of valence electrons which can be described with

$$E_p = \hbar \left(\frac{ne^2}{\epsilon_0 m} \right)^{\frac{1}{2}} \tag{1.13}$$

where E_p is the plasmon energy loss, $\hbar$ is the reduced Planck constant, n is the free electron density of the material, ϵ_0 is the permittivity of free space, e is the charge of the electron and m is the mass of the electron.

Core Loss Region. Core loss peaks occur from the interaction of the incident electrons with inner shell electrons. During this interaction, the energy transfer from the incident electrons causes the core electrons to become excited and move to unoccupied energy levels. These peaks appear within the energy spectrum at energy losses >50 eV and are element specific (Figure 1.2).

Each peak or ionization edge is labeled by the original orbital level occupied by the core electron. For example, K edges are the result of excitation of 1s electrons and L_1, L_2, and L_3 edges are the result of 2s, $2p_{1/2}$, $2p_{3/2}$ excitations respectively [10]. The nomenclature for transitions is shown in Figure 1.3.

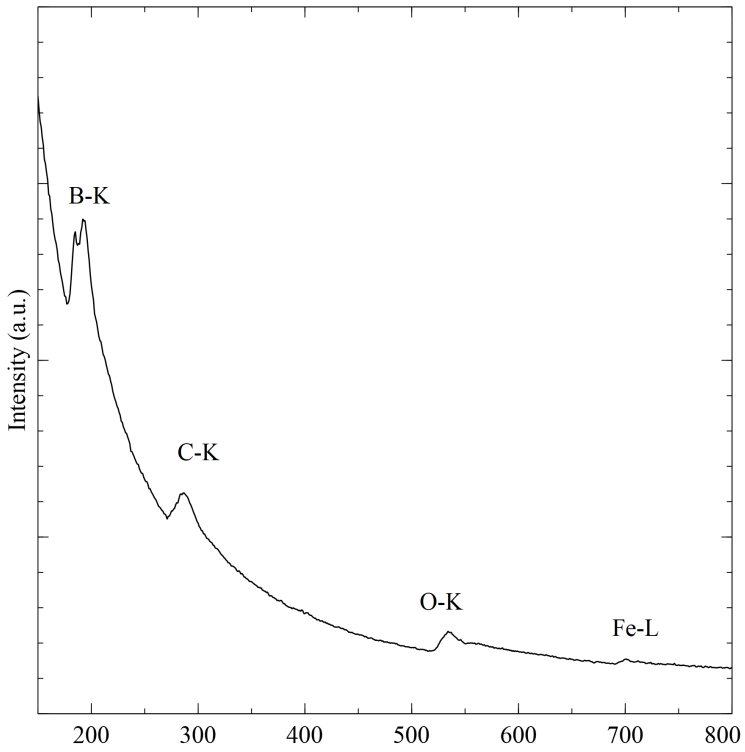

Figure 1.2: Example of core loss region with labeled core loss edges.

Core loss edges can take multiple shapes depending on the edge and the element. K-edges are defined as hydrogenic or "sawtooth" which is a sharp intensity followed by a gradual decay of intensity. Another edge shape is a delayed maximum, approximately 10-20 eV after the ionization threshold, that occurs in $L_{2,3}$ edges in third-period elements [4]. The third edge shape occurs most notable in transition metals and is called "white lines", which are sharp ionization threshold edges. Due to spin-orbit coupling, a split between the L_2 and L_3 edges with the L_2 edge having a higher energy threshold. The ratio of these peaks is based on the relative occupancy of the initial-states and can be used to determine valence states of a transition metal [9].

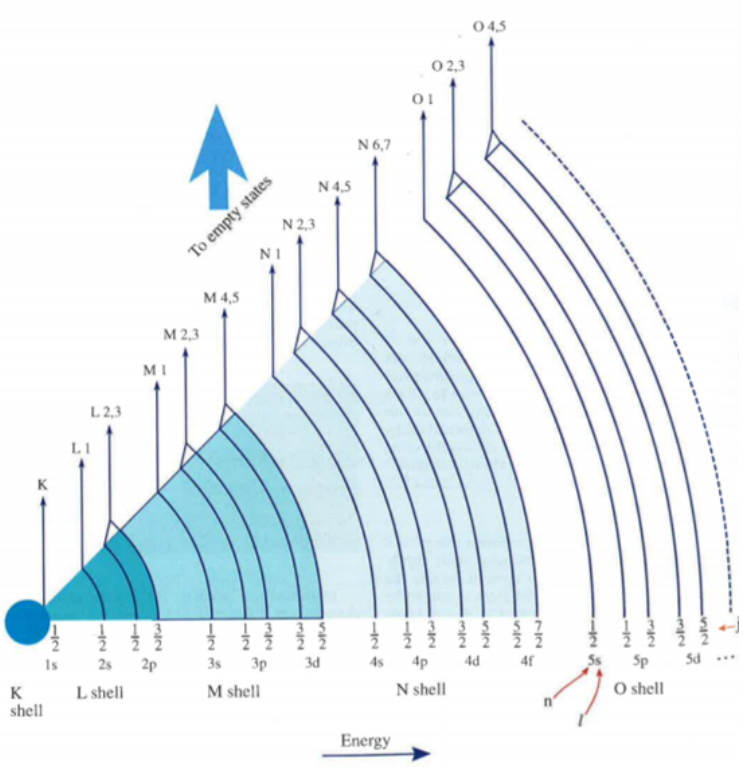

Figure 1.3: Diagram showing the nomenclature for core loss edges [10].

1.2.2 Energy Dispersive X-Ray Spectroscopy

When the electron beam inelastically interacts with the sample, incident electrons can impart energy and cause core electrons to ionize. This creates a vacancy in the atomic shell that is filled by a higher energy atom. In response to this vacancy, a higher energy electron will fill the hole releasing excess energy. The excess energy can be released as an x-ray with an emission energy being the difference between the initial and final state as shown in Figure 1.4.

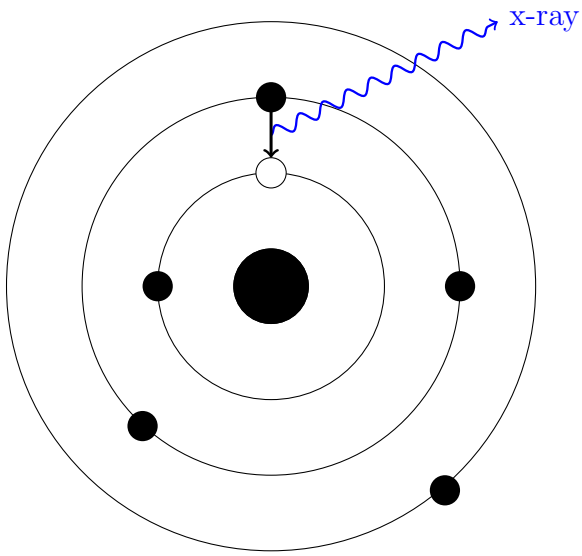

Figure 1.4: Atomic model showing the emission of a characteristic x-ray when a higher energy electron fills a vacancy of a lower energy shell. The energy of the x-ray is quantified as the difference of the initial (ϕ_i) and final shell(ϕ_f): $E_{x-ray} = \phi_i - \phi_f$ [11].

These x-rays are called characteristic x-rays and because the energy depends on the difference in shell energies, the energies are a monotonic function of Z [10]. This is described by Moseley's law

$$\lambda = \frac{B}{(Z-C)^2} \tag{1.14}$$

where B and C are constants related to the transition [11]. Moseley's law relates atomic number (Z) to λ which can be directly related to energy through $E = \frac{hc}{\lambda}$, where h is Planck's constant and c is the speed of light in a vacuum. This gives a final description of E as a function of Z to be:

$$E = \frac{hc(Z-C)^2}{B} \tag{1.15}$$

In order to generate a vacancy, the incident electrons have to impart enough energy to ionize the atom. The energy required is referred to as the binding energy or critical ionization

energy (E_c) [11]. This binding energy is related to binding of the electrons, such that K-shell electrons require more energy to eject than L-shell electrons. It also increases with Z due to the higher amount of protons binding the electrons to the atom [10].

To readily differentiate between the generated x-rays, the characteristic x-rays are labeled corresponding to the state of the vacancy created by the incident electron (K, L, M), with an additional label (α and β) indicating the initial state of the transitioned electron [10]. For example, a K_α x-ray occurs when an L electron drops into a vacancy in the K-shell while a K_β is when an M electron drops into the K-shell. Figure 1.5 shows allowed transitions and the resulting characteristic x-rays [10].

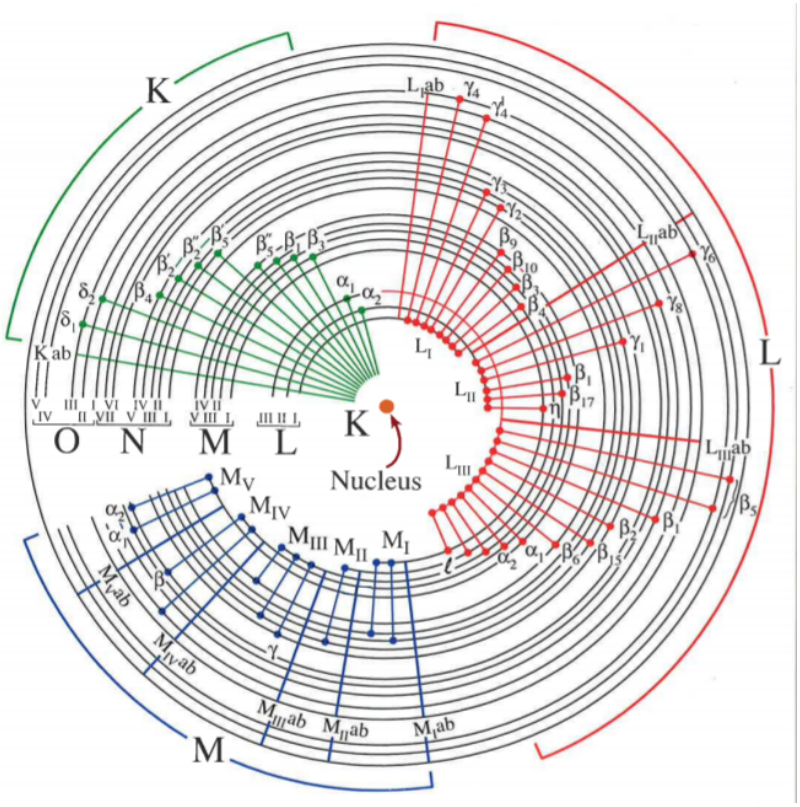

Figure 1.5: Allowed transitions that result in K, L, and M characteristic x-rays [10].

1.2.3 Mössbauer Spectroscopy

Mössbauer spectroscopy, another analytical technique, probes electronic and magnetic properties of the sample using resonantly absorbed γ-radiation. For iron Mössbauer spectroscopy, an energetic ^{57}Fe core is used as a source to resonantly emit γ radiation into a sample containing iron. The energy of this γ-ray is approximately 14.4 keV due to the transition of states from 3/2 to 1/2. For the Mössbauer experiment, the source and sample are moved at relative velocities and transmitted γ-rays are plotted as a function of this velocity [12]. For iron, the Doppler shift is on the order of a few mm/s in order to probe all the possible states of iron within a sample.

Three major parts of the Mössbauer spectrum are of interest when determining the state of iron within the sample. These are the isomer shift, electric quadrupole splitting, and the magnetic hyperfine interaction.

The isomer shift (δ) is the amount of Doppler shift applied to the source in order for the resonant absorption of γ-rays due to the Coulomb interaction between the nucleus and electrons [13]. This interaction causes a shift in energy levels without altering electron degeneracy, which is compensated for by the Doppler shift of the source (Figure 1.6.

The electric quadrupole interaction stems from the non-spherical charge distribution surrounding the nucleus interacting with an electric field gradient in the nucleus. Two sources are considered to contribute to the field gradient: charges on ions surrounding the Mössbauer atom, called lattice contributions, and anisotropic distribution of electrons in the valence shell of the Mössbauer atom [12]. This causes a splitting in the spectrum between electrons of spin-3/2 and spin-1/2 (Figure 1.6).

Hyperfine splitting occurs when a magnetic field interacts with the magnetic dipole of the electrons, when $S > 0$ as described by the Zeeman effect [14]. For iron, this causes the

s=3/2 to split into states (m_s = ±3/2; ±1/2) and the s=1/2 to split into two states (m_s = ±1/2). Figure 1.6 shows both the magnetic splitting and the resulting transitions due to magnetic hyperfine splitting. These transitions can be seen within the Mössbauer spectrum.

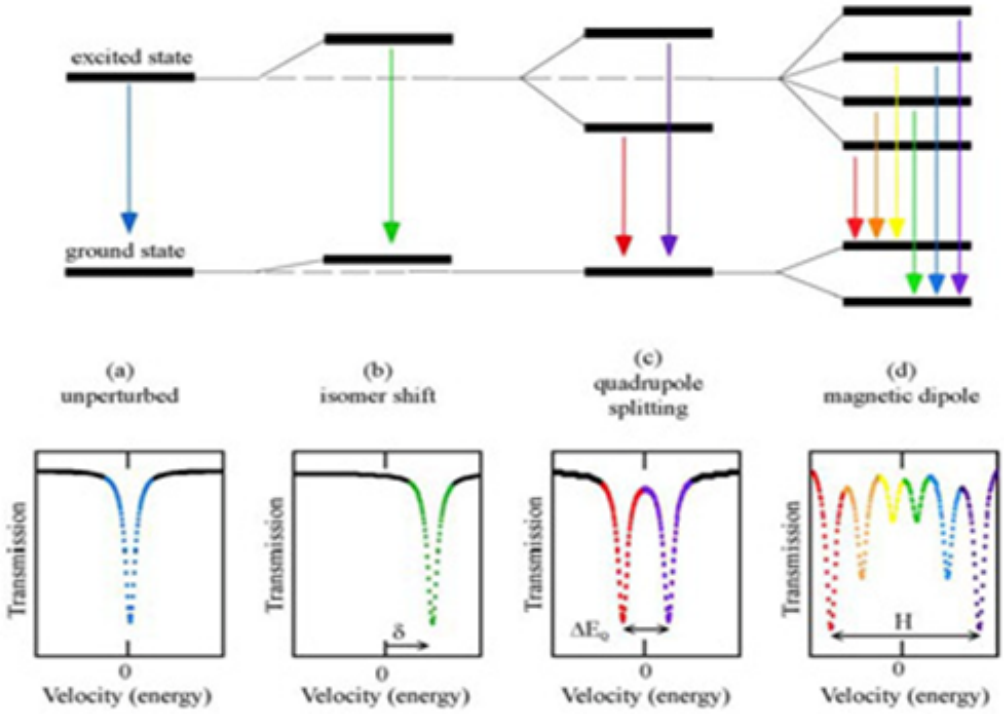

Figure 1.6: Diagram showing the hyperfine parameters and their effect on the Mössbauer spectrum [15].

1.3 Thesis Goals

The goal for this thesis is to analyze valence states of pure iron oxide nanoparticles through EELS and make direct comparisons to Mössbauer spectroscopy within a singular sample set. A boron nanoparticle sample will be analyzed to show the purity of the sample and create an EELS spectrum standard for comparison of the boron/iron oxide nanoparticles. Boron/iron oxide nanoparticles will be analyzed with XEDS to determine a qualitative elemental distribution of the sample. A quantitative analysis using EELS will determine the core/shell structure and valence state of the iron oxide shell. Fe_3O_4 has been shown to have an L_3:L_2 ratio of 5 [16, 17]. The iron oxide particles studied in this paper have an intensity ratio corresponding to the literature intensity of Fe_3O_4. Mössbauer spectrum analysis also indicates a valence structure consistent with Fe_3O_4 for the analyzed nanoparticles. The analysis of pure particles that composes the core/shell structure allows for more in-depth composition analysis of boron/iron oxide nanoparticles. The analysis of the boron/iron oxide nanoparticles confirmed the presence of the core/shell structure, the purity of the boron core, and the shell valence state as Fe_3O_4.

CHAPTER 2

EXPERIMENTAL

2.1 Instrumentation

2.1.1 TEM/STEM

There are three important components within the analytical electron microscope. These are the electron source, the lens system, and the detectors. Electron sources exist in two different varieties, thermionic and field emission. Thermionic sources function by heating a filament, usually made of Lanthanum hexaboride (LaB_6) [10]. The microscopes used in this study were equipped with field emission guns (FEGs) so that will be the focus of this portion. Field emission guns operate by applying a voltage (V) to a fine tip of radius, r, which produces a large electric field (E) on the tip. This is described by the following equation:

$$E = \frac{V}{r} \tag{2.1}$$

In order for the FEG to produce an accelerated electron beam, two anodes are placed below it. The first anode provides enough voltage to extract the electrons (called the extraction voltage) and the second accelerates the extracted electrons to the desired voltage.

After the beam is extracted, it progresses through the electron microscope column and needs to be focused. This is accomplished through the use of magnetic lenses, which function as an analog to optical lenses focusing light. The magnetic lens alters the initial path of the

electrons and causes them to move in a helical manner down the column, with a radius described by

$$r = \frac{\left[2m_0E\left(1+\frac{E}{2E_0}\right)\right]^{\frac{1}{2}}}{eB} \tag{2.2}$$

where m_0 and E_0 are the rest mass and energy of the electron, E is the energy of the electron, e is the charge of the electron and B is the magnetic field applied to the beam by the magnetic lens [10].

Apertures can be inserted into the lenses to help control different characteristics of the images, such as resolution, contrast and the collection angle of the electrons. These functions as physical barriers that narrows the electron beam. Much like optical lenses, the magnetic lenses are not perfect and contain spherical and chromatic aberrations. Spherical aberrations occur due to the stronger bending effect the lens has on electrons the farther they are from the optical axis. Chromatic aberrations occur due to the inhomogeneity of the electron energy source. These aberrations are a major limitation on the resolution within the TEM [10].

The STEM is equipped with multiple detectors that have the capability to be run in parallel. This capability is shown in Figure 2.1 and is possible due to each detector using different portions of the post-sample beam.

The EELS detector uses small-angle inelastically scattered electron beam and passes it through a magnetic spectrometer. In a similar manner to the magnetic lenses, the magnetic spectrometer bends the electrons according to the Lorentz force law. Slower electrons are bent more because they spend more time within the magnetic field before hitting a charged couple device (CCD) detector. Each pixel on the CCD detector stores charges generated by the electrons which then gets converted into a spectrum and is related to a specific energy value. This relation is what allows for the plotting of intensity vs energy loss used in EELS.

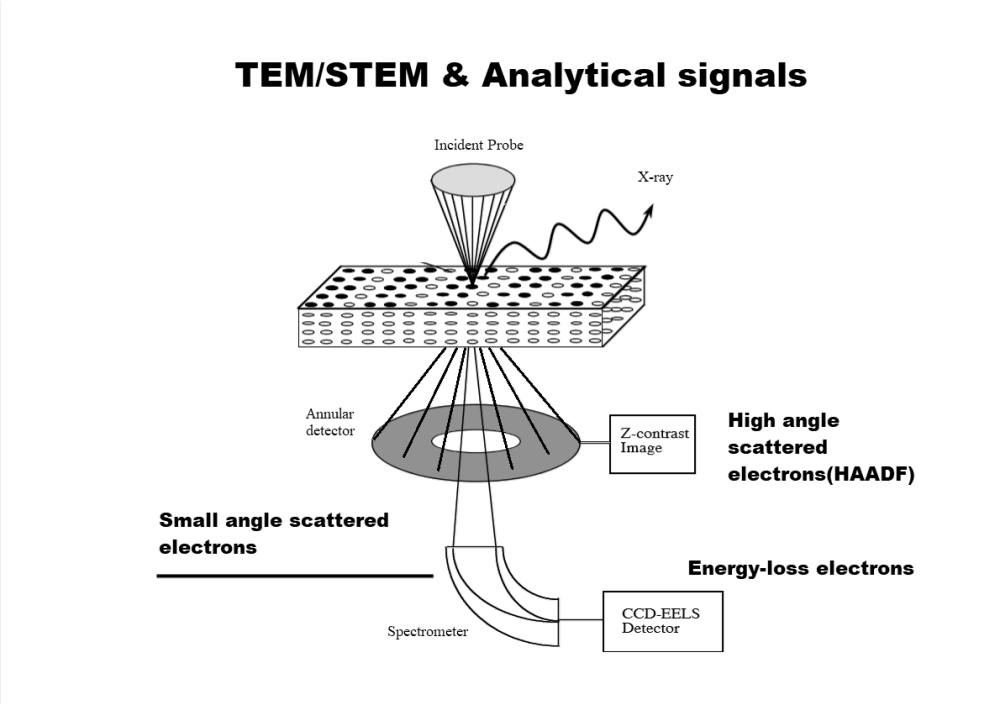

Figure 2.1: Detector setup for analytical electron microscope [18].

The high angle annular dark field (HAADF) detector collects high angle elastically scattered electrons and are used to form Z-contrast images. As described in chapter 1, the elastic scattering in the TEM is proportional to Z^2. Because of the Z^2 dependence, changes in composition across the sample can be visibly seen within an image.

The XEDS detector equipped on the microscope used in this study is called a silicon drift detector (SDD). The SDD is a series of ringed p-doped silicon implanted on a single crystal of n-doped silicon [10]. The SDD functions similarly to a CCD by using the electrons generated by the x-rays on the silicon to create a signal.

For this study, two TEM/STEM microscopes equipped with a Schottky field emission electron gun operating at 200keV were used: FEI Tecnai F20ST and FEI Talos. The FEI Tecnai was used for the collection of HAADF images, EELS spectrum, and XEDS spectrum. The FEI Talos was used for the collection of HAADF images and high speed, high-resolution XEDS spectrum.

2.1.2 XEDS

As mentioned above, XEDS mapping and spectrum were collected using the FEI Talos equipped with a Super-X, 4SDD XEDS system at an extraction voltage of 200kV at Argonne National Laboratory CNM facility. Along with direct imaging, the FEI Talos allows for elemental mapping of samples. As described in Section 1.2.2, characteristic x-rays are generated and these x-rays are collected to create a spectrum of x-ray count vs. x-ray energy (Figure 2.2). In the STEM, spectra are collected in a raster scan and each spectrum is correlated to

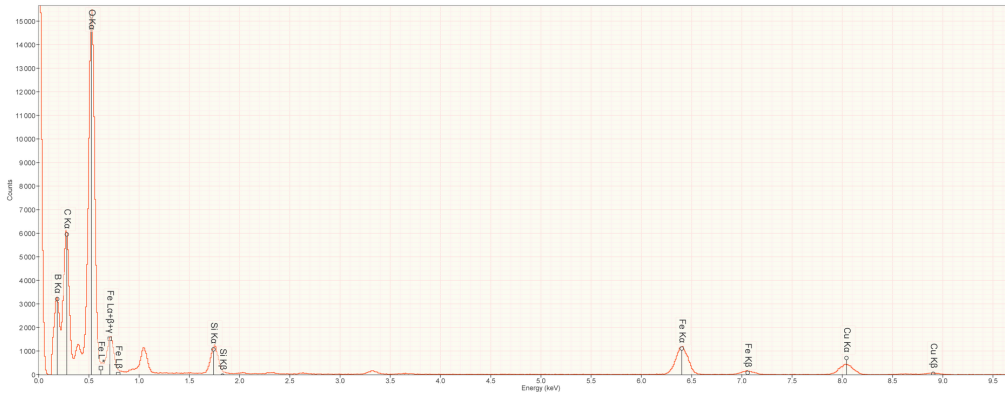

Figure 2.2: Example XEDS spectra plotting x-ray count vs. x-ray energy (keV).

a specific x-y position in the image. This can be visualized as a data cube, where points in the XY plane correspond to pixels in an image and the z-axis is the generated spectrum for that pixel (Figure 2.3) [10].

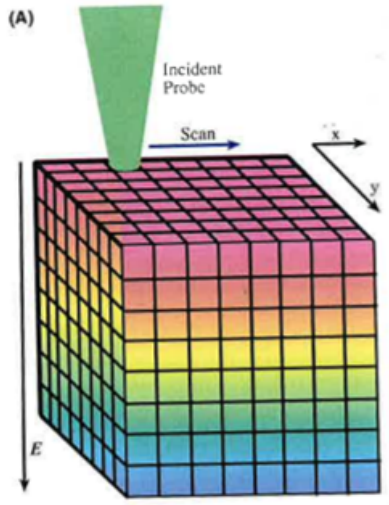

Figure 2.3: Visualization of the data cube. In relation to XEDS, the XY plane represents the pixel location with the Z-axis representing the spectrum generated at the specific pixel [10].

Since each pixel in the image has a corresponding spectrum, this information can be used to generate an elemental mapping of the analyzed image as shown in Figure 2.4. Due to a low signal-to-noise ratio for a single pixel's spectrum and the qualitative XEDS analysis used in this study, XEDS results come from areas of the mapped image plotted as a spectrum rather than viewing single pixel spectrum.

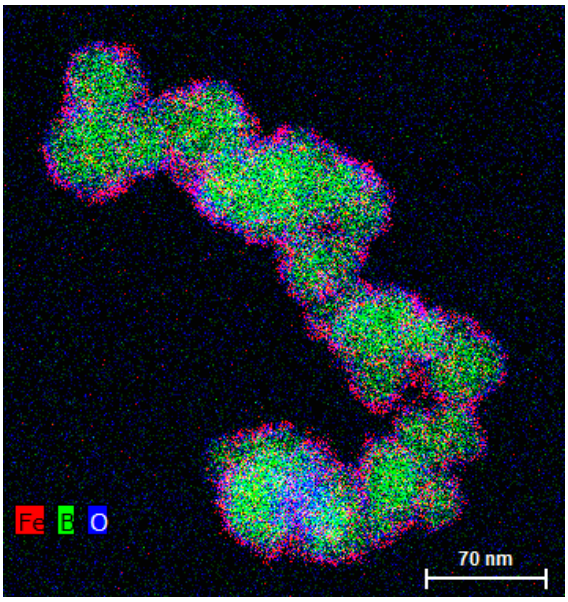

Figure 2.4: Example XEDS mapping showing the elemental distribution of iron (red), boron (green), and oxygen (blue).

2.1.3 EELS

EELS spectrum were collected within the FEI Tecnai F20ST in STEM-EELS mode at 200 keV extraction voltage using a Gatan parallel EELS spectrometer at Argonne National Laboratory CNM facility. For collection of the spectrum, a 70μm C2 aperture was used for a convergence half-angle of 2.5mrad. The acceptance half-angle was 7.7mrad from a 3mm GIF aperture and 100mm camera length.

As part of the analysis for the EELS spectrum, background subtraction was performed on each spectrum by fitting an AE^{-r} fit in a 30eV pre-edge window. An example of this fitting along with the pre- and post-background subtraction plot is shown in Figure 2.5. This EELS spectrum is processed in this manner for each desired edge within a spectrum. The boron nanoparticles will require a single background subtraction to analyze the boron K-edge, while the iron oxide particles will require two background subtractions, one for the oxygen

K-edge and one for the iron L-edge. In this manner, the boron/iron oxide nanoparticles will require three pre-edge background subtractions to individually analyze the boron K-edge, the oxygen K-edge, and the iron L-edges.

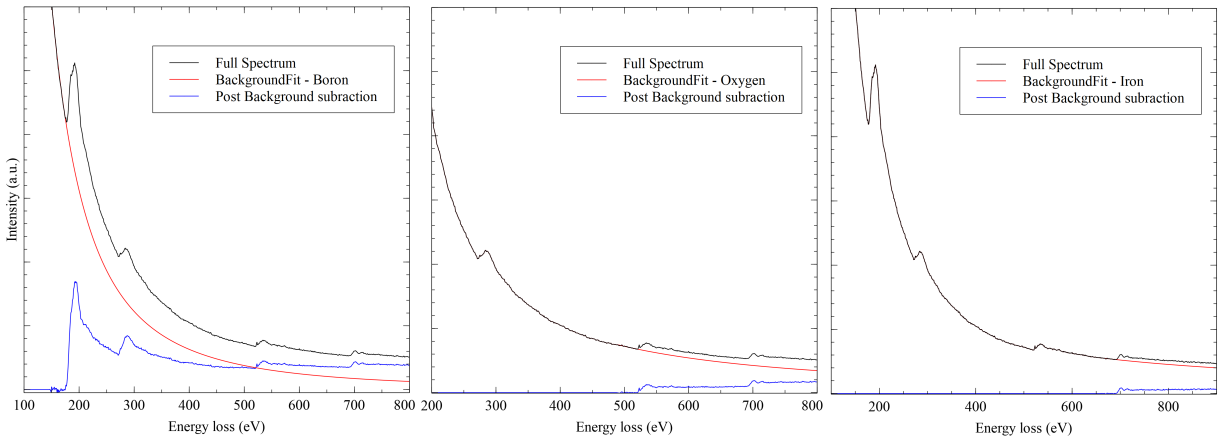

Figure 2.5: Example plots showing the initial spectrum, background fit, and background subtracted spectrum for boron, oxygen, and iron (Left to right).

Quantification of Fe^{3+}/Fe^{2+} is determined by comparing the ratio of integral intensity under the L_3 to L_2 peaks after background subtraction and fitting an arctan function (Figure 2.6).

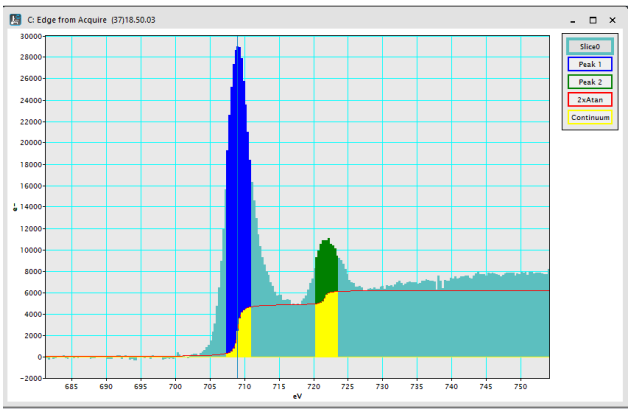

Figure 2.6: Arctan fit used to analyze the L_3/L_2 to quantify the valence structure of the iron oxide.

The arctan function is shown as the red curve in Figure 2.6 and is defined as follows

$$f(\Delta E) = \frac{h_1}{\pi}[arctan(\frac{\pi}{w_1}(\Delta E_1 - E_1)) + \frac{\pi}{2}] + \frac{h_2}{\pi}[arctan(\frac{\pi}{w_2}(\Delta E_2 - E_2)) + \frac{\pi}{2}] \qquad (2.3)$$

where the h_1 and h_2 are the heights of the arctan functions at the minima behind the L_3 and L_2 peaks, E_1 and E_2 are the inflection points widths of w_1 and w_2 of the L_3 and L_2 peaks respectively. ΔE_1 and ΔE_2 are the integration windows set to the full width at half maximum for the L_3 and L_2 peaks and can usually be set as $\Delta E_1 = \Delta E_2 = \Delta E$ [9].

2.1.4 Mössbauer Spectroscopy

Mössbauer data collection was done at Northern Illinois University in collaboration with Dr. Dennis Brown. For data collection, the Mössbauer spectrum was initially collected using an iron foil was fit and used as a calibration file for the analysis of the iron oxide nanoparticles (Figure 2.7). ^{57}Co was utilized as the radioactive source to generate the excited ^{57}Fe for Mössbauer spectroscopy analysis. The radioactive source was placed on a Mössbauer drive operating at 11mm/s to generate the Doppler effect needed for resonant absorption. A Mössbauer spectrometer was placed after the sample to collect γ-rays emitted from the sample. For sample preparation, 19.3mg of the iron oxide was mixed with 53.8mg of ground carbon to create an even distribution of iron oxide in the Mössbauer sample. Data for this sample was collected for seven days at a count rate of 1387 counts/sec.

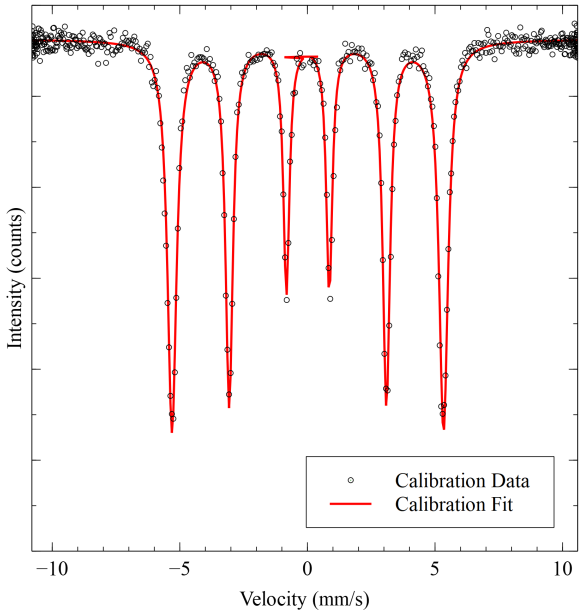

Figure 2.7: Mössbauer Calibration data.

2.2 Samples

The samples described in this section are all part of samples used in the Hosmane research group using synthesis methods, where applicable, to maximize the sample efficiency for the use in BNCT research. Aggregation was a point of concern during the creation of TEM samples. A script utilizing Python code was attempted to calculate the average settling time of a singular nanoparticle, but due to Reynold's number approximation, the time for a single nanoparticle was undetermined. It was found that nanoparticles behave under Brownian motion until large enough aggregates are formed [19]. To minimize the aggregation of the sample, it was collected in a pipette while the sample was being sonicated.

2.2.1 Iron Oxide Nanoparticles

The iron oxide nanoparticle samples analyzed in this study were synthesized by John Wozny and Nitya Nagarajan of the Hosmane group. The synthesis was done by initially adding Iron(III)- and Iron(II)-chlorides to deionized water then sonicated. Ammonium hydroxide (NH_4OH) was then added dropwise to the iron-chloride solution and stirred. The final product was centrifuged, dried then stored under argon.

To prepare the sample for analysis in the STEM, .0114g of iron oxide sample was dispersed in 6.05mL of 95% ethanol/5% deionized water. This solution was sonicated for 30 minutes at 40kHz with 2 drops of solution placed twice on the TEM grid. Upon imaging within the TEM, it was determined that the high solution concentration would interfere with analysis (Figure 2.8). Therefore a lower concentration of the sample was created. The initial concentration of the sample was $1.88\text{x}10^{-3}$ $\frac{g}{mL}$. 2mL of this solution was added to 4.5 mL of 95% ethanol/5% DI to create a new 6.5mL sample with a lower concentration of $6.23\text{x}10^{-4}$ $\frac{g}{mL}$. This lower concentration sample was used for the EELS analysis for this study.

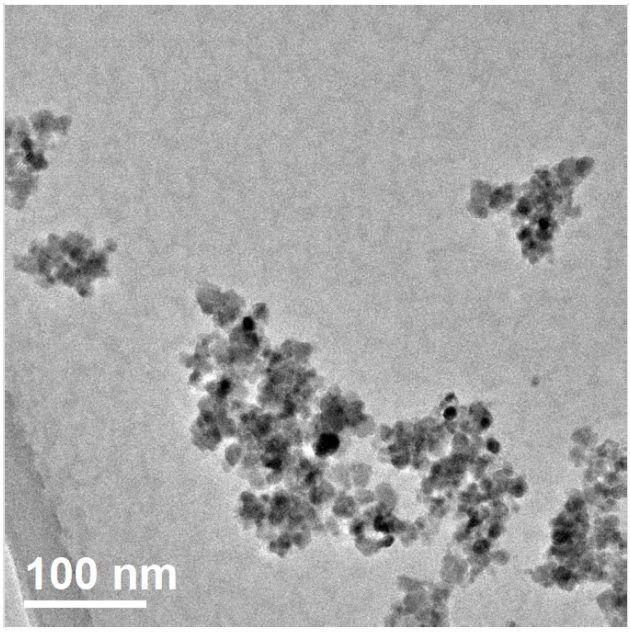

Figure 2.8: Bright field image of the initial high concentration iron oxide sample.

2.2.2 Boron Nanoparticles

The boron nanoparticles analyzed in this study were synthesized by Dr. Eyrusalam Bedasso during her doctoral studies at Northern Illinois University. To form the boron nanoparticles, Decaborane ($B_{10}H_{14}$) vapor underwent a gas phase pyrolysis at 1 atm in argon gas and 700-900 C over six hours [20, 3]. For TEM preparation, .0040g of boron nanoparticle was placed in 12.0mL (concentration of 3.33x10^{-3} $\frac{g}{mL}$) and sonicated at 40kHz for 30 mins. After 30 mins of sonication, the sample was extracted using a pipette and a single drop was placed on a TEM grid and allowed to air-dry.

2.2.3 Boron/Iron oxide Nanoparticle (Core/Shell Structure)

The boron/iron oxide nanoparticles analyzed in this study were synthesized and prepared for TEM analysis by Dr. Eryusalem Bedasso of the Hosmane group during her doctoral studies at Northern Illinois University. The core/shell sample was formed using co-precipitation of $FeCl_3 \cdot 6H_2O$ and $FeCl_2 \cdot 4H_2O$ with ammonium hydroxide (NH_4OH) in the presence of the boron nanoparticle to create an iron-oxide shell. The sample was dispersed in ethanol and sonicated at 60% amplitude for two minutes. One drop of the sonicated sample was placed on a TEM grid and left to dry. This was repeated two additional times [3].

CHAPTER 3

RESULTS AND DISCUSSION

3.1 Analysis of Iron Oxide Nanoparticles

Images of the iron oxide sample were taken to determine an average size of the iron oxide nanoparticles (Figure 3.1). The nanoparticles show an aggregation into clusters which occurs during the preparation of TEM samples. This aggregation will also be affected by the magnetic properties of the nanoparticles. Particle size ranged from 9 to 18 nm with an average of approximately 12 nanometers.

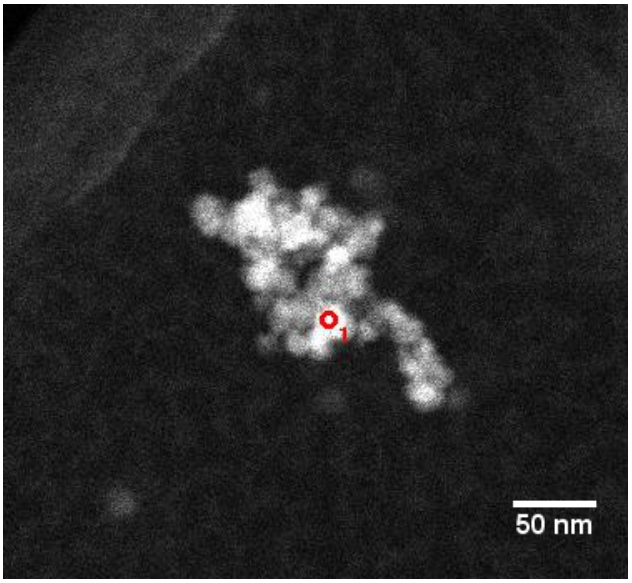

Figure 3.1: HAADF image of pure iron oxide nanoparticle cluster.

Two spectroscopy techniques were used to analyze the composition of the iron oxide nanoparticle sample. EELS and Mössbauer analysis was conducted on the same sample of

synthesized iron oxide nanoparticles in order to independently determine the valence state and composition of the sample.

3.1.1 EELS

In the molecular orbit frame, Fe_3O_4, the iron d orbital hybridizes with the oxygen p orbital. This allows electron transitions to this hybridized state, specifically the oxygen $1s$ to $2p$ and iron $2p$ to $3d$. Both of these transitions reflect the density of the d orbital in the iron [9, 21]. This results in the oxygen K-edge and iron $L_{2,3}$ edge in the EELS spectrum, which is detailed in Figure 3.2.

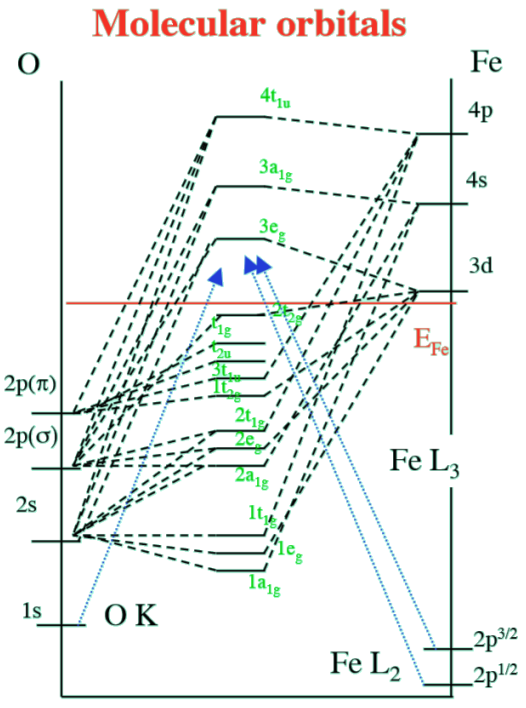

Figure 3.2: Hybridization of oxygen s-orbital and iron p-orbitals.

EELS spectra were collected from multiple nanoparticle clusters. Background subtraction was performed on each spectrum by fitting a function of the form AE^{-r} in a 30 eV window before the peak onset. These spectra were plotted and are shown in Figure 3.3. As stated above, the L_3 and L_2 edges correlate to $2p^{3/2}$ and $2p^{1/2}$ respectively. The L_3 maximum has been shifted to 709.5eV to compensate for a spectrum shift that occurs within the EELS spectrometer [9]. The shifting of the peak maximum removes the ability to measure chemical shifts as described in Van Aken *et.al* [9]. Qualitatively, the Fe-$L_{2,3}$ spectrum have a similar shape which indicates consistency across the sample.

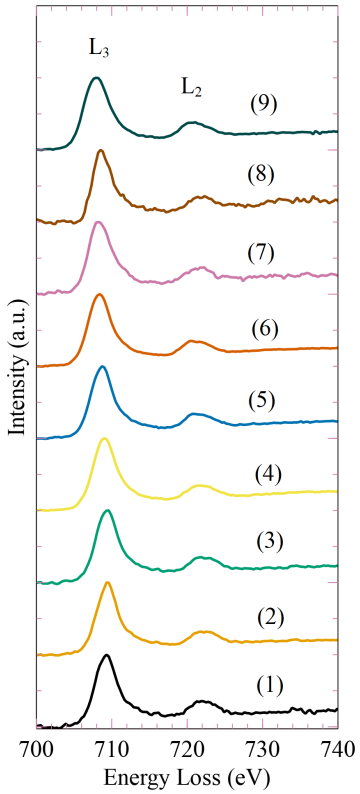

Figure 3.3: EELS spectrum of Iron L-edges collected from iron oxide sample. Each spectrum is labeled for reference.

The L_3/L_2 intensity ratio was calculated after fitting each spectrum to the arctan function Eq. 2.3 with a 3 eV window. These values are tabulated in Table 3.1. The calculated ratios range from 4.7 to 5.4 with an average of 5.0. Within the calculated error, the L_3/L_2 intensity

ratio has a high agreement with literature [16, 17] that provides an iron oxide structure indicative of Fe_3O_4.

Spectrum	L_3/L_2 Intensity Ratio
(1)	4.7
(2)	5.1
(3)	5.0
(4)	5.3
(5)	4.8
(6)	5.1
(7)	5.4
(8)	5.0
(9)	4.9
Average L_3/L_2	$5.1 \pm .2$
Cavé [16]	$5.00 \pm .09$

Table 3.1: Calculated L_3/L_2 intensity ratios for the iron oxide nanoparticle sample.

In conjunction with the L-edge analysis, oxygen K-edges were analyzed and compared to the literature (Figure 3.4). The analyzed oxygen spectra were used to create a basis for comparison to the core/shell structure oxygen K-edge analyzed later. Within the oxygen K-edge, there is a definitive intense prepeak at the peak onset, which occurs due to the hybridization of oxygen 1s and iron 2p orbitals as seen above in Figure 3.2. In comparison to literature, the oxygen K-edges for the analyzed sample show a strong similarity to that of the Fe_3O_4 oxygen K-edge found in the literature [21]. There is a large noise signal in the analyzed oxygen K-edge, therefore a higher energy resolution and signal to noise ratio is needed to conclusively determine the valence structure of the iron oxide from the oxygen K-edge.

It was determined from the EELS analysis of the Fe-$L_{2,3}$ and O-K edges that the valence state of the iron oxide nanoparticles strongly correlates to that of Fe_3O_4 but further analysis is needed to conclusively indicate this structure.

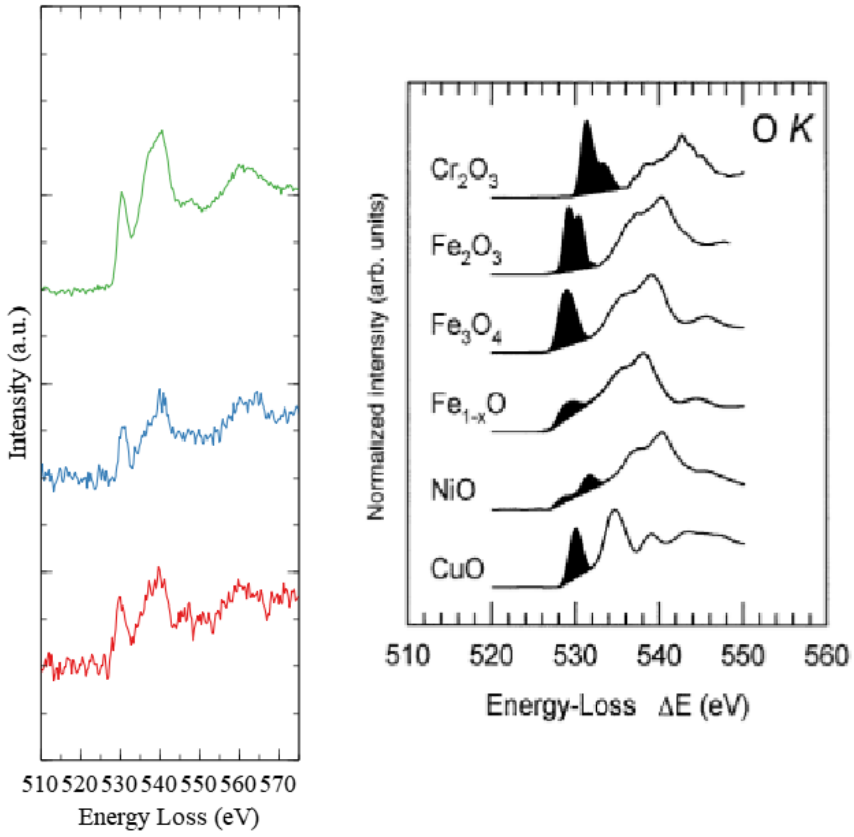

Figure 3.4: Left: Oxygen K-edge of analyzed iron oxide nanoparticles. Right: Oxygen K-edge for different transition metal oxides [21]

3.1.2 Mössbauer Analysis

Along with EELS analysis, Mössbauer spectroscopy analysis was conducted on the same sample of iron oxide. The 3-site fit corresponds to an A-site containing Fe^{3+} and a B-site which contains both Fe^{3+} and Fe^{2+} within Fe_3O_4. These sites represent the location of iron within the crystallography as seen in Figure 3.5.

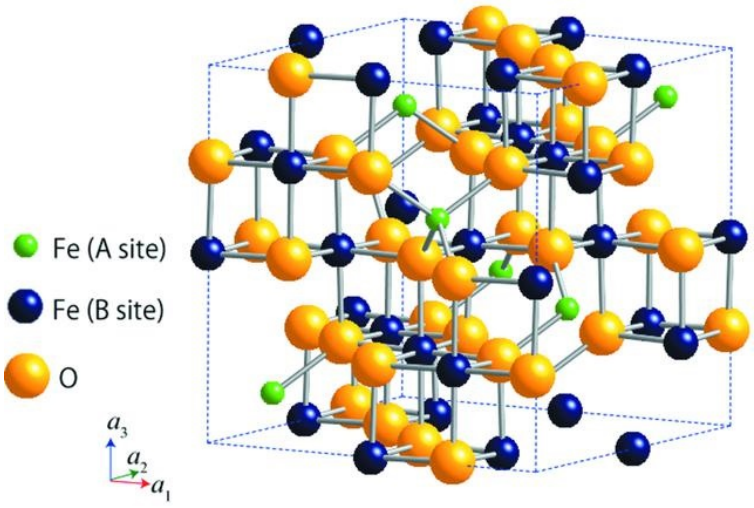

Figure 3.5: Overview of Fe_3O_4 A and B sites within the crystal structure [22].

The spectrum with the 3-site fit is detailed in Figure 3.6. The magnetic fields were determined to be 46.9 T and 39.7 T for the ferromagnetic A and B sites respectively, which has been tabulated in Table 3.2.

Site 2 is a paramagnetic iron state. Its isomer shift indicates that its valence state is Fe^{3+}. Due to a fitting for Fe^{3+} and Fe^{2+} within the sample, this is an indicator that the iron oxide sample is most likely Fe_3O_4. Fe_3O_4 is the only common structure that contains both Fe^{3+} and Fe^{2+}.

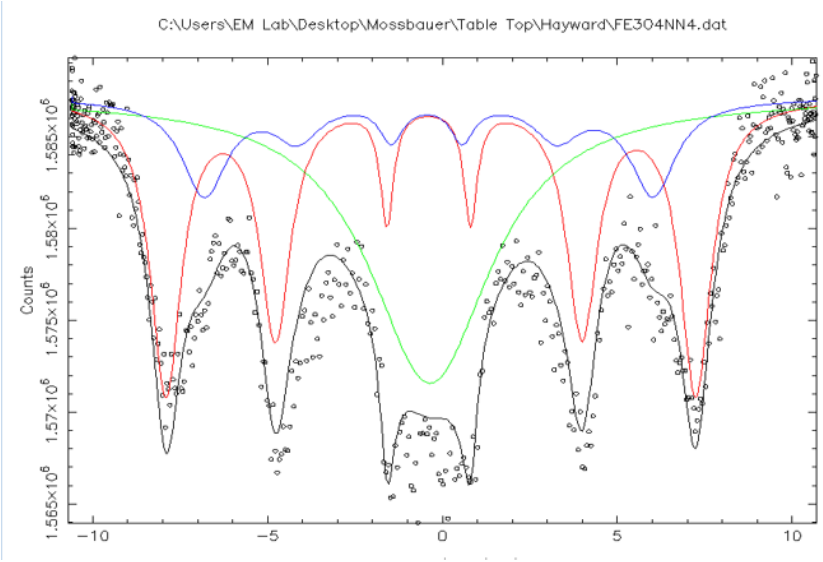

Figure 3.6: Mössbauer spectrum of Fe_3O_4 showing 3-site fit. Site 1 (red) corresponds to the Fe^{3+} within the A-site. Site 3 (blue) corresponds to the Fe^{3+}/Fe^{2+} B-site and Site 2 (green) is Fe^{3+} in a nonmagnetic state.

The broadening of the spectrum may be due to superparamagnetic relaxation effects which occur in particle sizes on the order of 15nm. The analyzed sample has a distribution of particle sizes which will cause additional broadening in the spectral lines. Site 2, therefore, may arise due to relaxation effects of particles with sizes much smaller than 15nm. When particle size reaches approximately 5nm, the Mössbauer spectrum will collapse to a quadrupole doublet (Figure 3.7).

Mössbauer Analysis		
Site No.	B (T)	Isomer Shift (δ)
A site (Red)	46.9	.34
B site (Green)		.32
B site (Blue)	39.7	.37

Table 3.2: Summary of Mössbauer Analysis showing the magnetic fields and isomer shifts of each site fit.

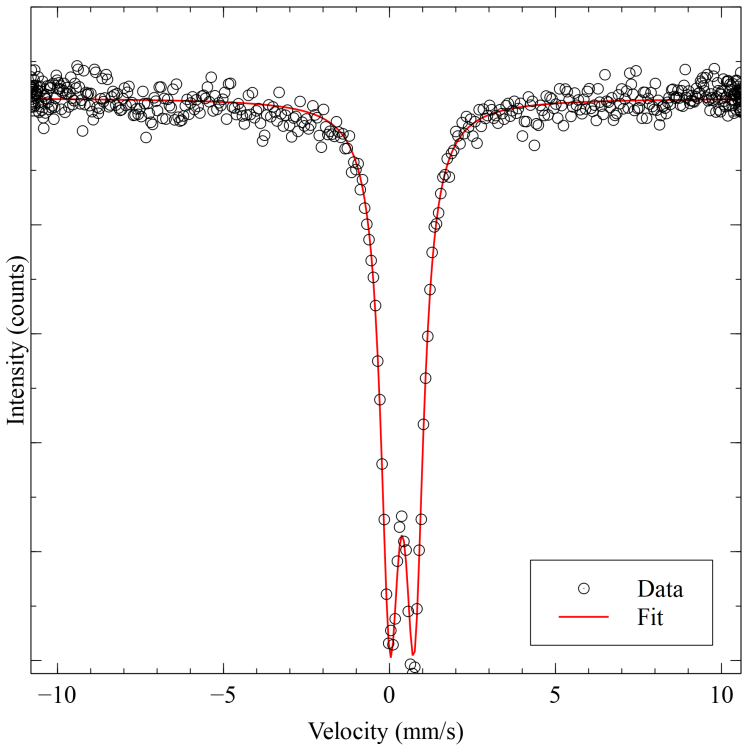

Figure 3.7: Mössbauer spectrum of quadrupole doublet indicative of superparamagnetism.

3.1.3 Summary

Iron oxide was analyzed using two different types of spectroscopic techniques. Within the calculated error, EELS analysis determines that the structure of the iron oxide is Fe_3O_4. Independently of this analysis, Mössbauer spectroscopy was also used to analyze the structure of the iron oxide sample. A Fe^{3+} and a $Fe^{2}+$ site were determined which leads to the determination that the structure should be Fe_3O_4. The results from the Mössbauer analysis combined with the results from the EELS analysis show the iron oxide sample analyzed is the Fe_3O_4 structure.

3.2 Analysis of Boron/Iron oxide Nanoparticle

3.2.1 Pure Boron Nanoparticle

An important part of BNCT is the quantity of neutron capturing boron that is exposed to the tumorous cells. Because of this, it is imperative that the boron contained in the core/shell structure is not oxidized during synthesis. To show the purity in the core/shell structures, boron nanoparticles were first imaged using the HAADF detector. The nanoparticle size ranged between 17nm and 25nm with an average of 21nm. The boron was then analyzed by EELS to construct an analytical standard for spectrum comparison. Characteristically, the boron K-edge onset appears at 188eV and pure boron will lack a strong prepeak that indicates orbital hybridization.

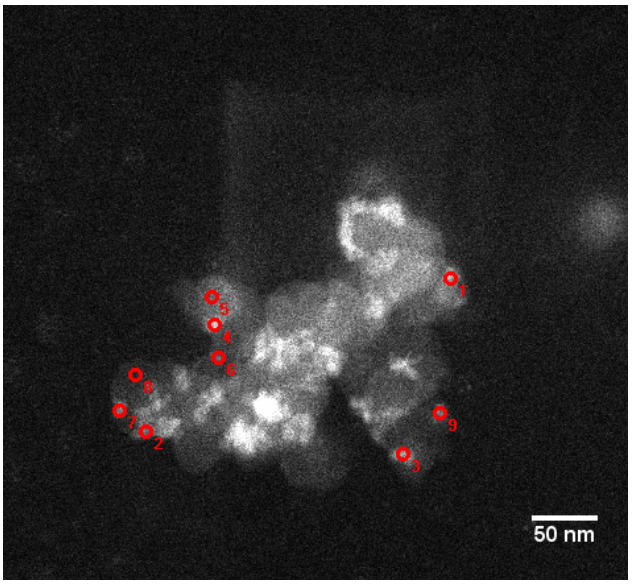

Figure 3.8: HAADF image of a boron nanoparticle cluster.

Figure 3.9 shows the boron K-edge collected from the boron nanoparticle sample in comparison to a pure boron and boron oxide (B_2O_3) EELS spectrum [23]. Noticeable in this

spectrum is the peak onset occurring at 188eV and the absence of an intense hybridization prepeak. Both sets of spectra are focused on the boron K-edge which shows the initial peak onset at 188eV, but the difference comes in the lack of intense peak that is apparent in the B_2O_3 spectrum. This confirms the unoxidized state of the boron nanoparticles to be used in the synthesis of core/shell nanoparticles. This also gives a standard for the boron K-edge which will be used in the analysis of the core/shell structure.

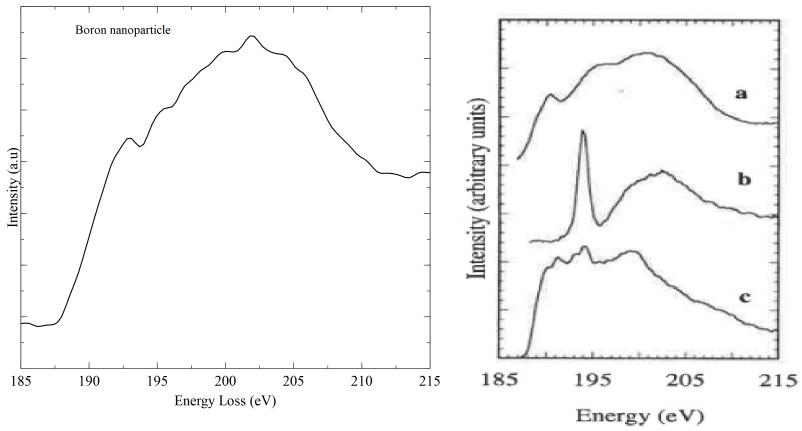

Figure 3.9: (Left) EELS spectra of analyzed boron nanoparticles. (Right) Analyzed boron K-edges from pure boron (a), B_2O_3 (b), and t-Ni_2B (c) [23].

3.2.2 Core/Shell Structure

The analysis of the core/shell structure involved the initial imaging of the sample prepared on the TEM grid. HAADF images were taken during the collection of XEDS and EELS spectra. Figure 3.10 shows a HAADF image taken during the collection of EELS spectra using the FEI Tecnai F20ST. The image was used to make measurements of individual nanoparticles, which ranged from 22nm to 36nm and averaged approximately 29nm. These

particles were analyzed using XEDS to create a qualitative elemental distribution map and EELS to confirm the state of boron and iron oxide within the core/shell structure.

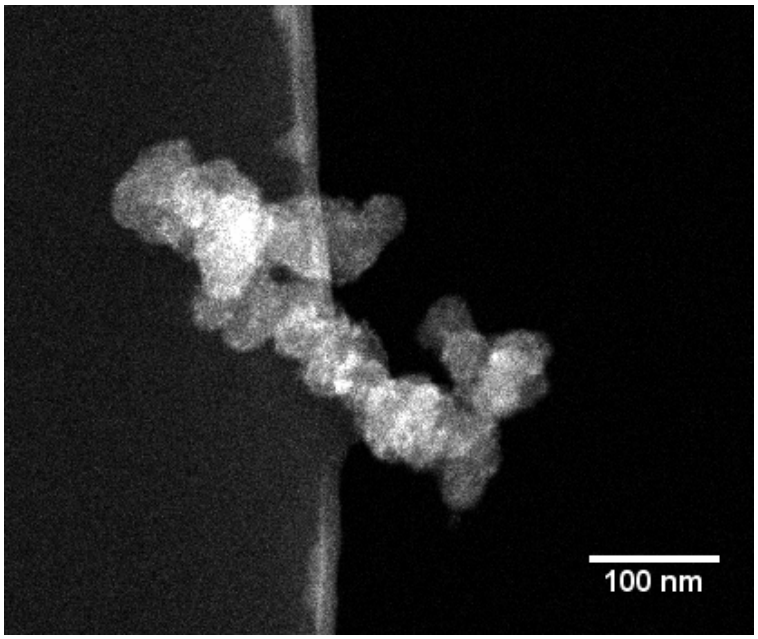

Figure 3.10: HAADF image of boron/iron nanoparticle cluster hanging at the edge of the carbon film.

3.2.2.1 XEDS

Qualitative XEDS mapping was initially performed on the core/shell structure to make an initial approximation of the structure of the boron/iron oxide nanoparticles. The mappings suggest that the iron oxide forms on an outer layer of the boron core as intended. A number of mappings are provided in this section with additional mappings included in Appendix B. Figure 3.11 shows the mapping of a core/shell nanoparticle cluster indicating the presence and general location of iron (red), boron (green), and oxygen (blue).

Figure 3.12 shows the same nanoparticle cluster with the iron and boron visible. This mapping offers a better view of the location of the iron around the boron. Since oxidation

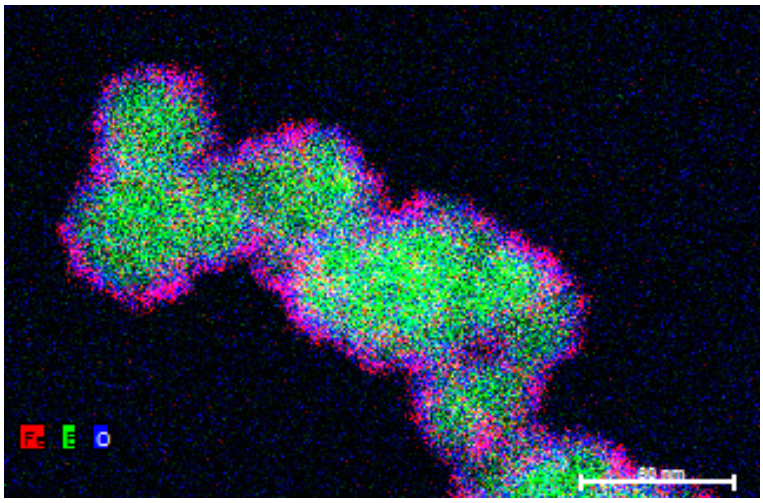

Figure 3.11: XEDS mapping of boron/iron oxide nanoparticle cluster showing the presence of boron, iron, and oxygen.

of the boron core is a concern for usage in BNCT, it is important to make a determination of the location of oxygen in relation to the boron and iron. Figure 3.13 shows the general location of oxygen within the nanoparticle cluster with iron as a reference. The oxygen has a similar structural pattern as the iron and appears to coat the boron. This creates an initial indicator that the oxygen is present in conjunction with the iron as a form of iron oxide.

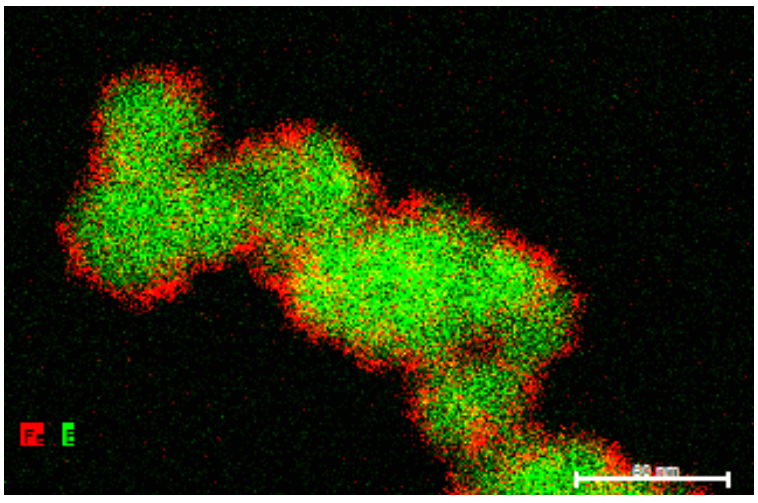

Figure 3.12: XEDS Mapping of iron and boron in the core/shell nanoparticle structure.

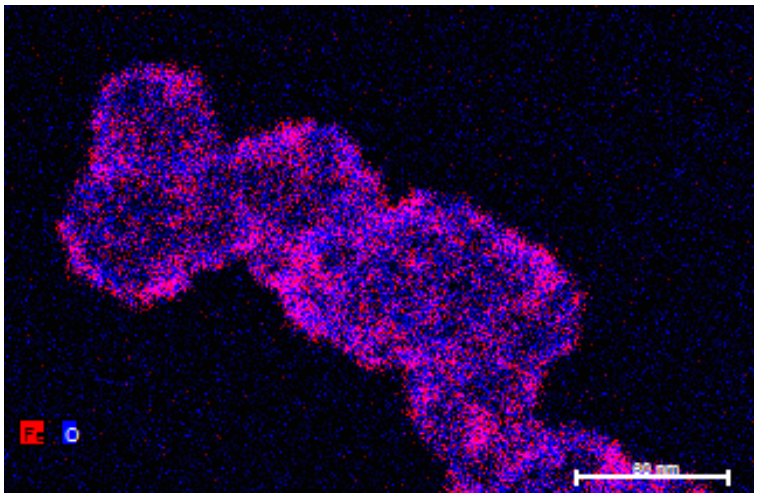

Figure 3.13: XEDS mapping of iron and oxygen in the core/shell nanoparticle structure.

While oxygen exhibits a structural pattern similar to the iron, a large presence of oxygen was found within a nanocluster which indicates a possibility of oxidation in the boron core (Figure 3.14). EELS analysis must be used to confirm the composition of the nanoparticle core.

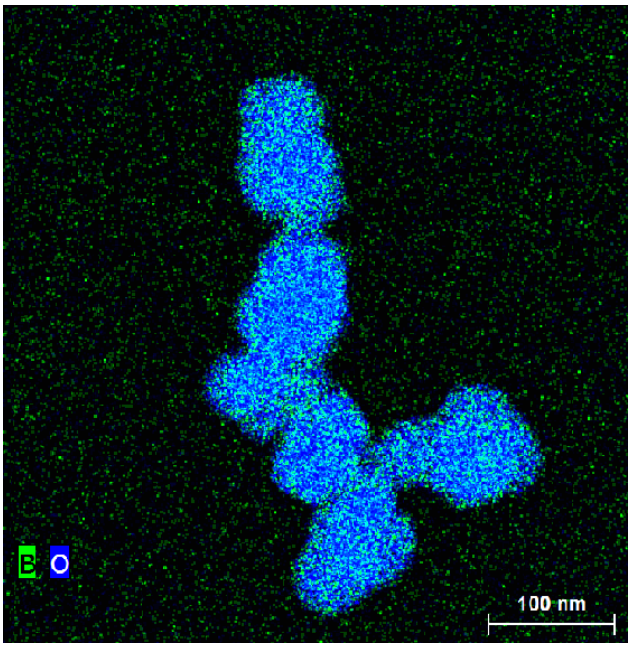

Figure 3.14: XEDS mapping of boron and oxygen in the core/shell nanoparticle structure. The large presence of oxygen indicates possible oxidation of the boron core.

Figure 3.15 shows another nanoparticle cluster mapped by XEDS. This cluster shows an inconsistency in the amount of boron coated by the iron oxide shell. The left portion of the cluster shows a lower concentration of boron coated by the iron when compared to the right portion of the nanoparticle cluster. This cluster also contains an area extremely rich with iron.

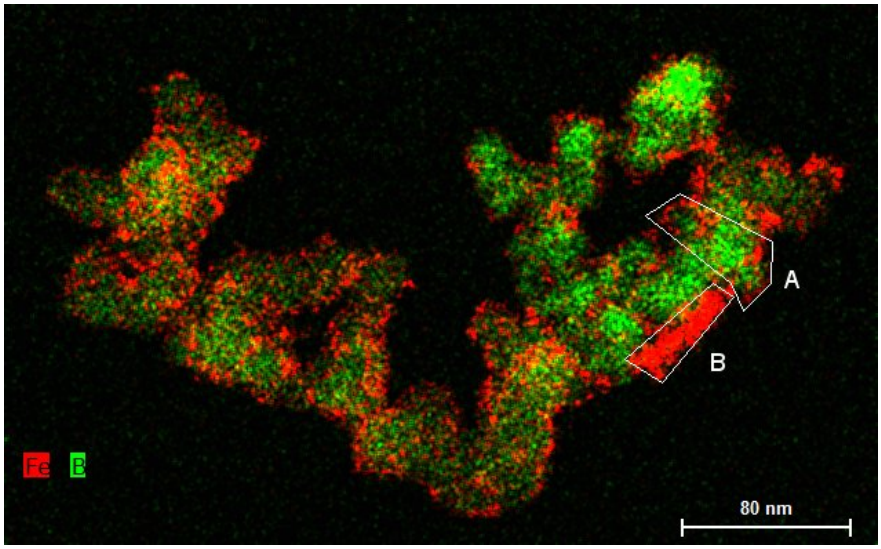

Figure 3.15: XEDS mapping of boron/iron oxide nanoparticle cluster.

Area A and B represent a typical boron/iron oxide area and the iron-rich area, respectively. The composite spectra of these areas were compared, as shown in Figure 3.16. As expected, area A contains a higher quantity of boron compared to iron. Area B has minimal boron with a much higher concentration of boron. Both spectra have a comparable amount of carbon, copper, and silicon which can be contributed from the TEM grids and silicon XEDS detectors.

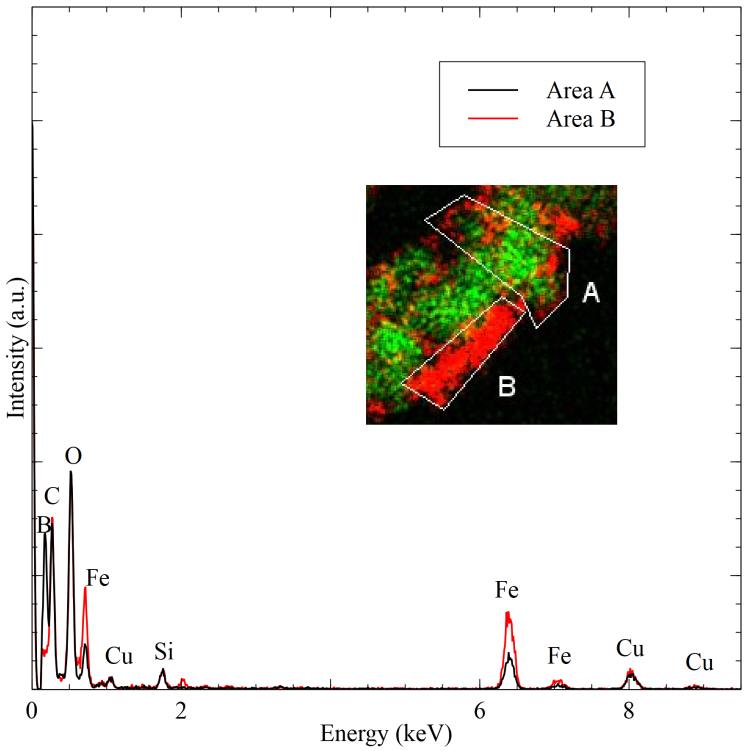

Figure 3.16: XEDS spectrum of boron/iron oxide nanoparticle cluster. Insert: Spectrum location on XEDS mapping

3.2.2.2 EELS

As with the iron oxide and boron nanoparticles, the core/shell nanoparticles were analyzed using EELS to confirm the valence state of the iron oxide shell and the bonding nature of the boron core. Figure 3.17 shows an EELS spectrum collected from the core/shell nanoparticle sample. Elements found within the spectrum are boron, carbon, oxygen, and iron. This corresponds to the composition results found in the qualitative mapping done by XEDS.

The core/shell boron K-edge has a similar structure to the boron nanoparticle sample indicating the boron remains unoxidized beyond detection limits. Another indicator that the boron is unoxidized is the shape of the oxygen peak. The oxygen K-edge has an intense

prepeak that indicates hybridization but it lacks any noticeable deformation from the oxygen K-edge in the iron oxide sample. We would expect a variation in the peak shape should bonding occurring due to the hybridization of between the oxygen and boron.

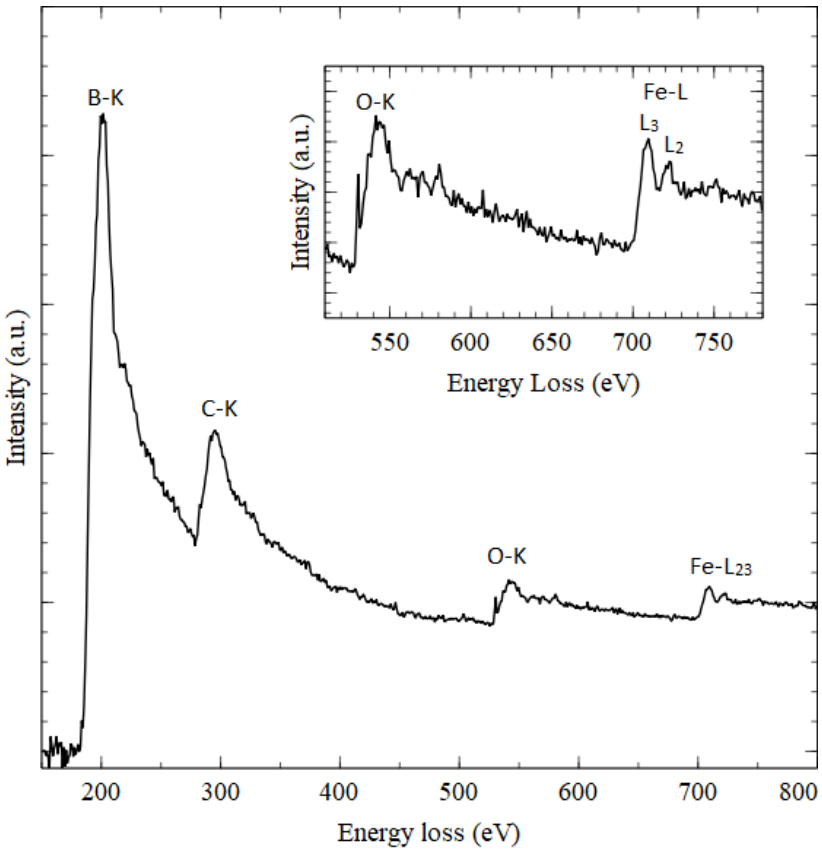

Figure 3.17: EELS spectrum of core/shell structure with labeled edges. Insert: Oxygen K-edge and Iron L-edges

An L_3/L_2 analysis was also performed on the core/shell structure to verify the iron oxide maintains its structure as Fe_3O_4. An average intensity ratio for the core/shell was determined to be $4.9 \pm .2$. Within the calculated error, the L_3/L_2 suggests that the iron oxide shell maintains its structure as Fe_3O_4 during the synthesis process of the core/shell structure.

3.2.3 Summary

In this section, boron nanoparticles were analyzed to create a standard for an unoxidized boron edge to be used in comparison in the core/shell analysis. The analysis of the core/shell structure involved the elemental mapping through XEDS to show that the iron oxide nanoparticles coat the boron to create the desired core/shell structure. After confirming the existence of the core/shell structure, an EELS analysis was completed to compare the boron K-edge, oxygen K-edge, and iron L-edge of the core/shell structure to the results of the previously analyzed pure nanoparticles. It was determined that the boron core remains unoxidized after the synthesis of the core/shell nanoparticle by comparison to the boron K-edge and oxygen K-edge. An L_3/L_2 calculation was conducted on the iron L-edge of the core/shell structure which resulted in an intensity ratio comparable to Fe_3O_4. This allowed for the determination that the iron oxide shell structure remains Fe_3O_4.

CHAPTER 4

CONCLUSIONS AND FUTURE WORK

Pure iron oxide and boron nanoparticles were analyzed to confirm both the composition of the nanoparticles and to create a comparison standard for the analysis of core/shell structured nanoparticles to be used in BNCT. The iron oxide sample was determined to be Fe_3O_4 through EELS analysis and confirmed by Mössbauer analysis, which independently showed an initial fit for multiple sites that mostly agree to that found in Fe_3O_4 [17]. The boron nanoparticles were shown that in the worst case scenario, oxidation occurs at a level that is undetectable through EELS analysis. Through the use of XEDS mapping, it was shown that the boron/iron-oxide nanoparticles consistently showed a shell of iron oxide surrounding a boron core, which was also confirmed during the EELS analysis. EELS analysis on the core/shell nanoparticles also showed that the bulk of boron particles within the core/shell structure appears to have remained as pure boron without oxidizing. In addition, an L_3/L_2 EELS intensity ratio was then performed and proved to be consistent with Fe_3O_4 that is also found in literature [16, 17].

The results of this study will lead to a continued analysis of boron/iron oxide core/shell structures using both EELS and Mössbauer as the synthesis process is adjusted to produce a more uniform distribution of size and composition. Magnetic susceptibility measurements will allow more information on the magnetic states of the iron oxide. A more in-depth study of the interface between the core/shell is required as that information will help to reveal structural information between the boron and iron oxide. As the particles become smaller, a more careful study in the magnetic properties may be required due to the superparamagnetic property that Fe_3O_4 obtains below 10 nm in diameter.

REFERENCES

[1] Martha Sibrian-Vazquez, and Maria da Graça H. Vicente, Boron Tumor Delivery for BNCT: Recent Developments and Perspectives. in *Boron Science: New Technology and Applications*, edited by Narayan Hosmane. CRC Press, Boca Raton, 2011.

[2] Christoph Alexiou, Roswitha J. Schmid, Roland Jurgons, Marcus Kremer, Gerhard Wanner, Christian Bergemann, Ernst Huenges, Thomas Nawroth, Wolfgang Arnold, Fritz G. Parak Targeting Cancer Cells: Magnetic Nanoparticles as Drug Carriers. *Eur Biophys J* 35, 2006, pp. 446-450.

[3] Eyrusalam Bedasso, *Boron-Based Nanostructures: Synthesis, Functionalization, and Characterization*. Ph.D. thesis, Northern Illinois University, 2015.

[4] R. F. Egerton, *Electron Energy-Loss Spectroscopy in the Electron Microscope*, 3rd ed. Springer, New York, 2011.

[5] Mitio Inokuti, Inelastic Collisions of Fast Charged Particles with Atoms and Molecules-The Bethe Theory Revisited *Reviews of Modern Physics* 43, 1971. pp. 297-347.

[6] Steven S. Zumdahl and Susan A. Zumdahl, *Chemistry* 8th ed., Brooks Cole, Belmont, 2010.

[7] Rik Brydson, *Electron Energy Loss Spectroscopy*, Taylor and Francis, London and New York, 2001.

[8] Harald Ibach and Hans Lüth, *Solid-State Physics: An Introduction to Principles of Materials Science* 4th ed., Springer, Berlin, 2009.

[9] P. A. van Aken, B. Liebscher, Quantification of Ferrous/Ferric Ratio in Minerals: New Evaluation Schemes of Fe L_{23} Electron Energy-Loss Near-Edge Spectra. *Phys. Chem Minerals*, 29, 2002. pp. 188-200.

[10] David B. Williams, C. Barry Carter, *Transmission Electron Microscopy*, 2nd ed. Springer, New York, 2009.

[11] J. C. Russ, *Fundamentals of Energy Dispersive X-ray Analysis*, Butterworths and Co, London, 1984.

[12] Phillip Gütlich, Rainer Link, Alfred Trautwein, *Mössbauer Spectroscopy and Transition Metal Chemistry*, Springer-Verlag, New York, 1978.

[13] Barrie A. Sosinsky, Aspects of Organoiron Mössbauer Spectroscopy in *Chemical Mössbauer Spectroscopy*, edited by R. H. Herber. Plenum Press, New York and London, 1984.

[14] David J. Griffiths, *Introduction to Quantum Mechanics* 2nd ed, Cambridge University Press, Cambridge, 2017.

[15] S. Thomas, Mössbauer Spectroscopy, https://serc.carleton.edu/NAGTWorkshops/mineralogy/mineral_physics/mossbauer.html.

[16] Lisa Cavé, Tom Al, Diana Loomer, Steven Cogswell, Louise Weaver, A STEM/EELS Method for Mapping Iron Valence Ratios in Oxide Minerals. *micron* 37, 2006, pp. 301-309.

[17] Ryan Hufschmid, Joachim Landers, Carolyn Shasha, Soma Salamon, Heiko Wende, and Kannan M. Krishnan, Nanoscale Physical and Chemical Structure of Iron Oxide Nanoparticles for Magnetic Particle Imaging *Phys. Status Solidi A* 216, 2019, 1800544.

[18] Courtesy of Nigel Browning, Robert Klie, and Yasuo Ito.

[19] D. D. Liyanage, Rajika J. K. A. Thamali, A. A. K. Kumbalatara, J. A. Weliwita, and S. Witharana, An Analysis of Nanoparticle Settling Times in Liquids *Journal of Nanomaterials*, vol. 2016, Article ID 7061838, 7 pages, 2016.

[20] Brian J. Bellott, Wontae Noh, Ralph G. Nuzzo, and Gregory S. Girolami, Nanoenergetic Materials: Boron Nanoparticles from the Pyrolysis of Decaborane and Their Functionalisation. *Chem. Commun.*, 2009, pp.3214-3215.

[21] P. A. van Aken, B. Liebscher, V. J. Styrsa, Core Level Electron Energy-Loss spectra of Minerals: Pre-Edge Fine Structures at the Oxygen K-edge *Phys Chem Minerals* 25, 1998, pp. 494-498.

[22] M. Okube, T. Yasue, S. Sasaki, Residual-density Mapping and Site-Selective Determination of Anomalous Scattering Factors to Examine the Origin of the Fe K Pre-Edge Peak of Magnetite *J. Synchrotron Rad.* 19, 2012, pp. 759-767.

[23] G. Mountjoy, A. Corrias, P. H. Gaskell, An Electron Energy Loss Spectroscopy Study of $Ni_{60}B_{40}$ Alloys Prepared by Chemical Reducation and Melt Spinning *Journal of Non-Crystalline Solids*, 192-193, 1995, pp. 616-619.

[24] Paul Cueva, Robert Hovden, Julia A. Mundy, David A. Muller, The Open-Source Cornell Spectrum Imager *Microscopy Today* 21, 2013, pp. 40-45.

[25] D. R. G. Mitchell, B. Schaffer, Scripting-Customised Microscopy Tools for Digital Micrograph^{tm} *Ultramicroscopy*, 103, 2005, pp. 319-332.

APPENDIX A

SOFTWARE

Detailed in this appendix is the software used for analysis in this study and a brief discussion on the specific usage.

ImageJ/Cornell Spectrum Imager (CSI) is an open source tool for ImageJ was used to analyze images and EELS spectrum collected during this study[24]. This tool was used for nanoparticle measurements in HAADF images and background subtractions of EELS spectrum.

Gatan Microscopy Suite (GMS) is a software developed by Gatan for processing of spectrum collected in the microscope. In conjunction with open source scripts developed by Dave Mitchell[25]. This combination was used to perform background subtractions and subsequent L_3/L_2 ratios on EELS spectrum.

Additional EELS analysis Matlab programs from *Electron Energy-Loss Spectroscopy in the Electron Microscope* by R.F. Egerton were used in learning background subtractions and deconvolutions of EELS spectra [4]. These programs were run in the GNU Octave software.

Mössbauer Data Analysis Program is a software initially developed by Robert Preston and maintained by Dennis Brown of Northern Illinois University. This software was for analysis of Mössbauer spectroscopy data including fitting the iron sites and parameterizing the magnetic field and isomer shift.

APPENDIX B

ADDITIONAL EDS SPECTRUM

Additional EDS mappings not provided within the body of this thesis are included within this appendix.

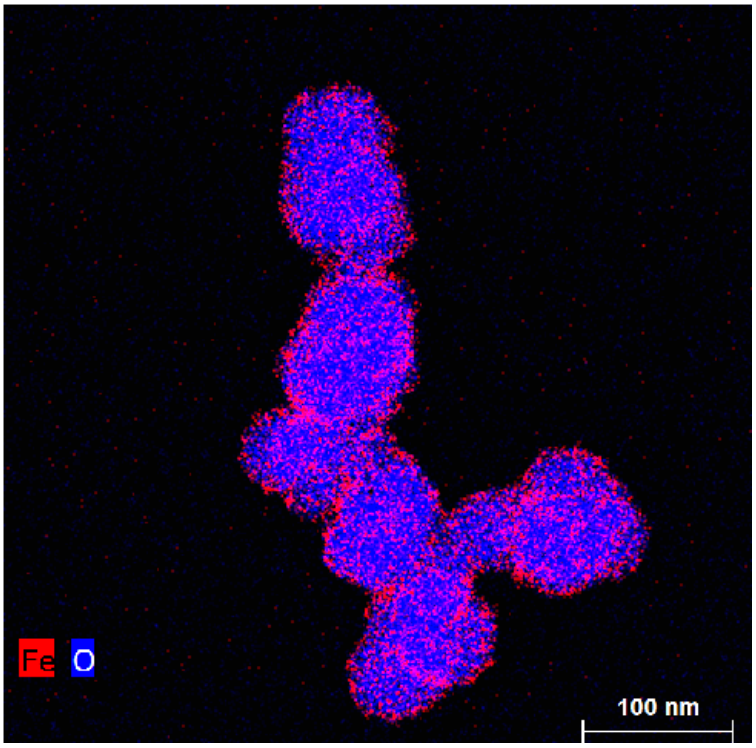

Figure B.1: EDS Mapping of nanoparticle cluster with iron (red) and oxygen (blue) shown. The high presence of oxygen indicates a possibility of oxidation within the core.

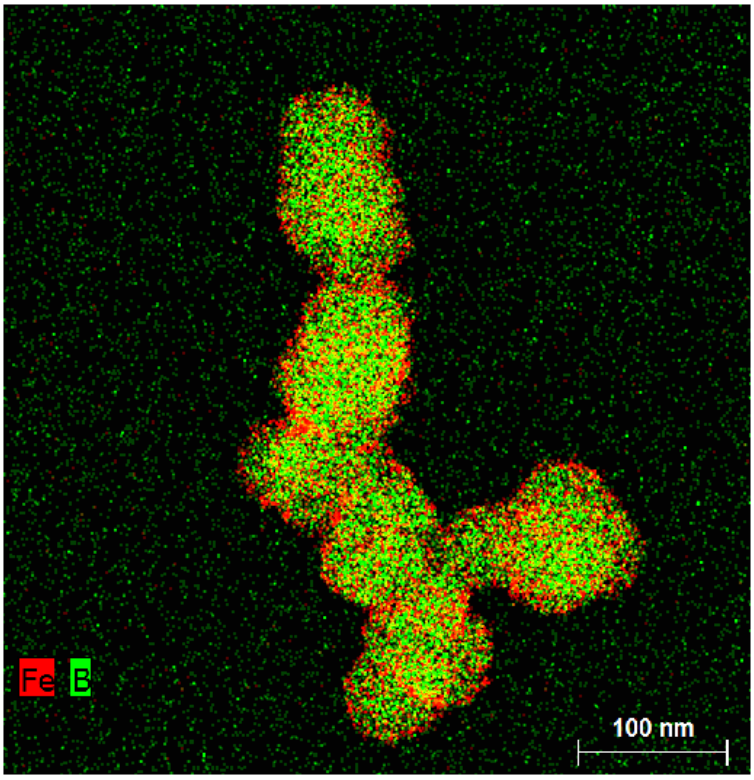

Figure B.2: EDS Mapping of nanoparticle cluster with boron (green) and iron (red) shown. The iron appears to coat the boron in this mapping indicating the presence of a core/shell structure.

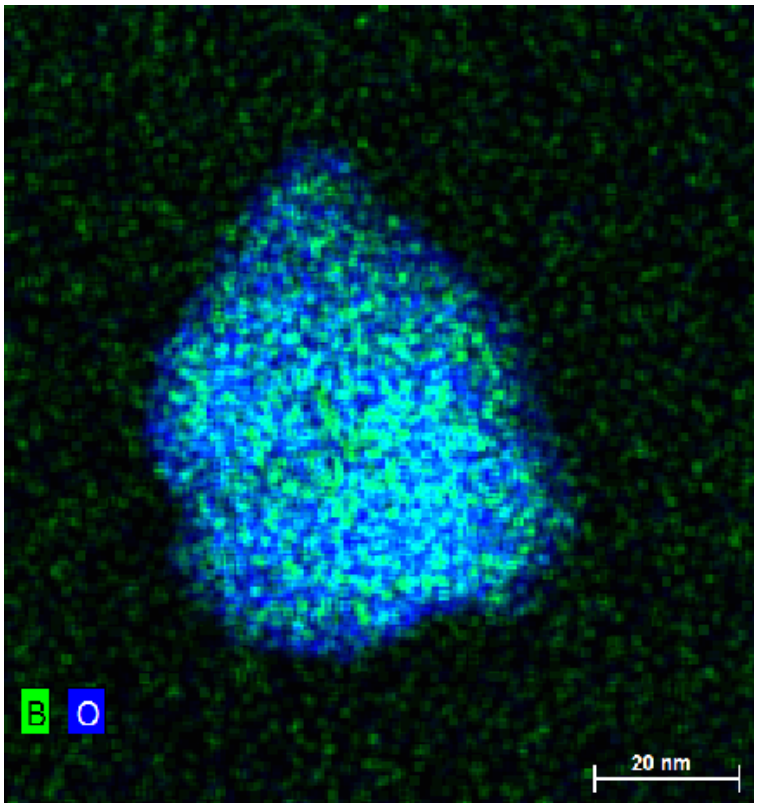

Figure B.3: EDS Mapping of small nanoparticle cluster with boron (green) and oxygen (blue) shown. A high presence of oxygen also contained in this mapping indicating possible oxidation.

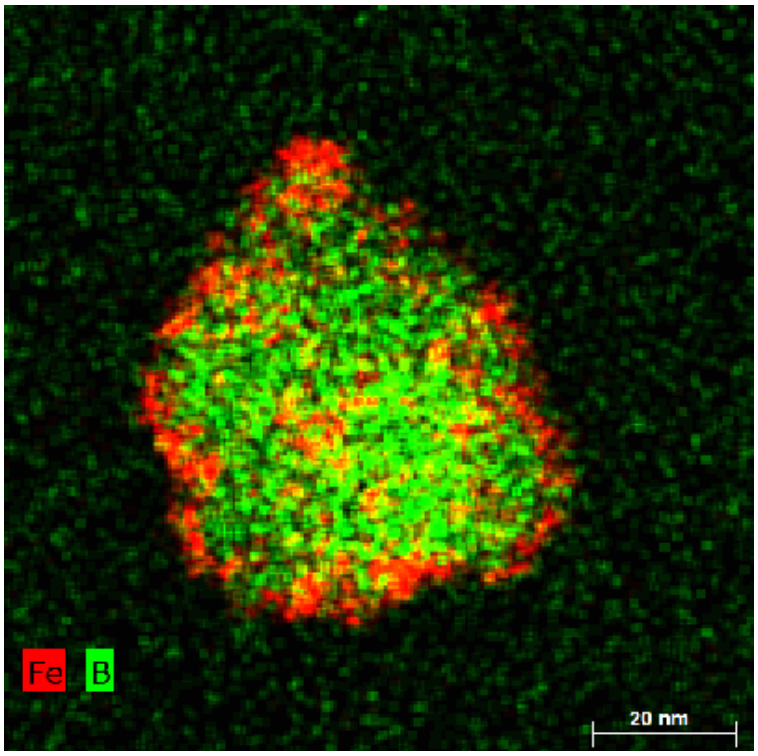

Figure B.4: EDS Mapping of small nanoparticle cluster with boron (green) and iron (red) shown. 5 individual core/shell structures are readily visible from this cluster.

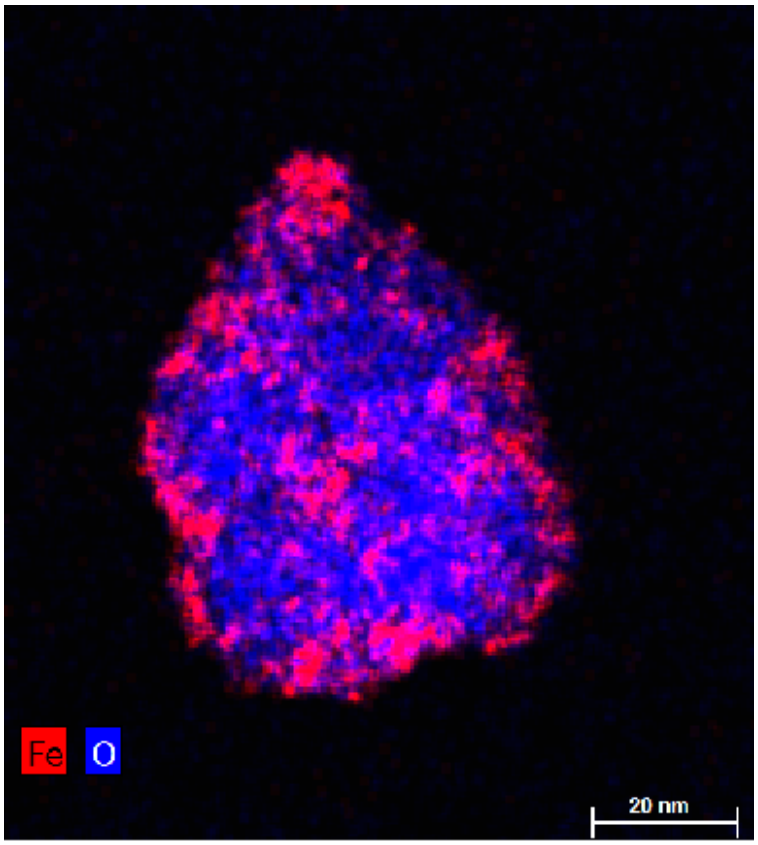

Figure B.5: EDS Mapping of small nanoparticle cluster with iron (red) and oxygen (blue) shown. Oxygen presence surrounding the entirety of the core/shell structure indicating possible oxidation of core.

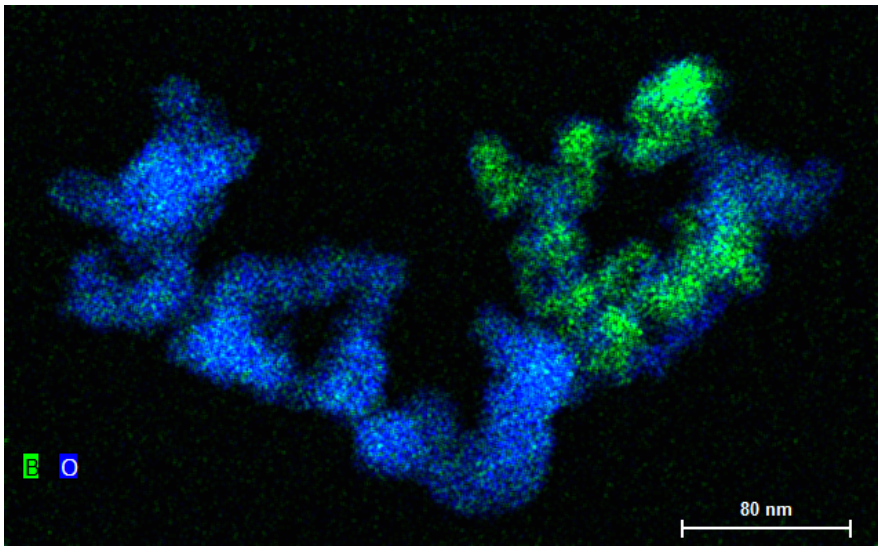

Figure B.6: EDS Mapping of nanoparticle cluster with boron (green) and oxygen (blue) shown. Non-uniform distribution of boron is readily visible across this nanoparticle cluster.

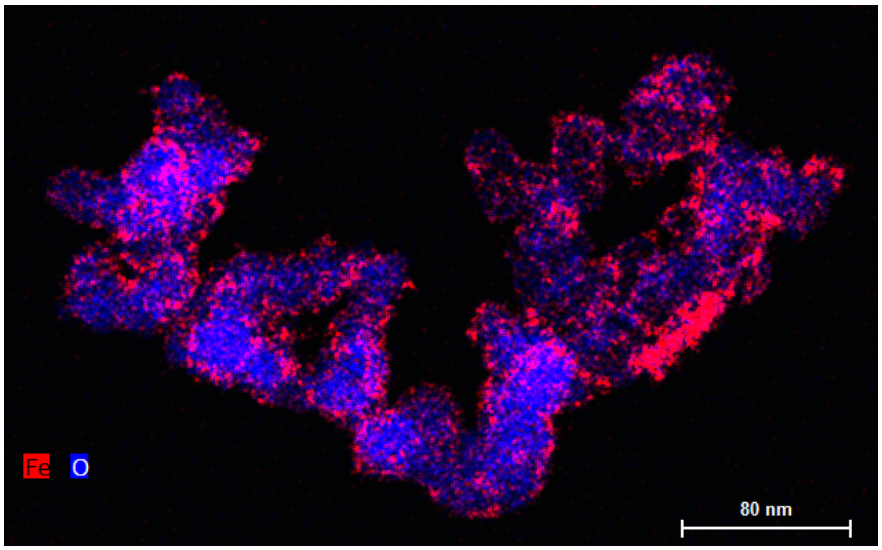

Figure B.7: EDS Mapping of nanoparticle cluster with iron (red) and oxygen (blue) shown. Non-uniform presence of oxygen in regards to oxygen indicates possible oxidation of core. The iron shell also exhibits a non-uniformity.

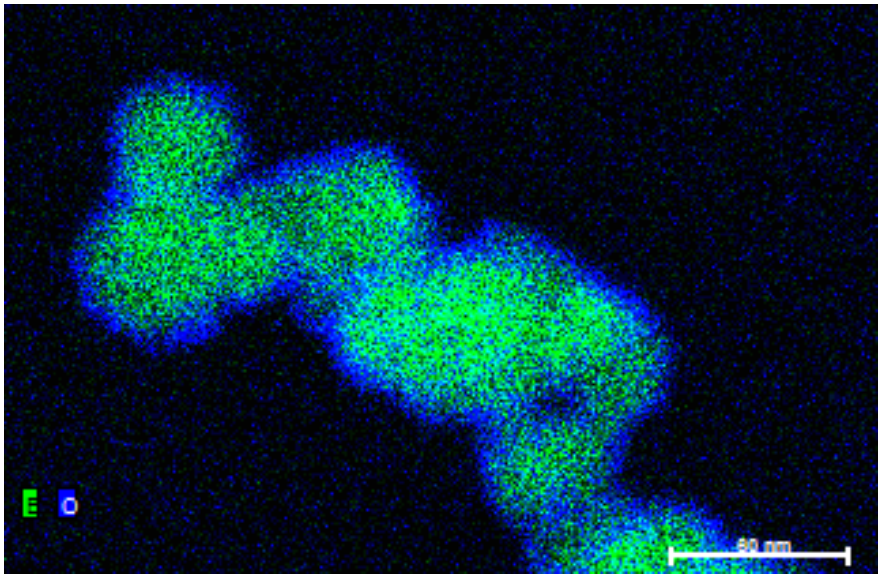

Figure B.8: EDS Mapping of nanoparticle cluster with boron (green) and oxygen (blue) shown. Oxygen distribution indicates a localization to the shell of the nanoparticle structure.